Spatial distribution of vegetation in deserts: quantification and impact on aeolian geomorphology
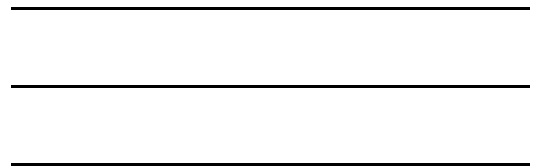
Ian Oliver McGlynn
Portsmouth, Virginia

B.S., George Washington University, 2003

A Thesis presented to the Graduate Faculty
of the University of Virginia in Candidacy for the Degree of
Master of Science

Department of Environmental Sciences

University of Virginia
May, 2006

_____

_____

_____

Abstract

Mineral dust aerosols suspended in the atmosphere impact atmospheric radiative transfer, global and oceanic nutrient cycling, cloud formation and precipitation. The entrainment of dust in desert environments is highly sensitive to vegetation cover that can reduce erodibility and stabilize surfaces. It is essential to understand the relationship of geospatial patterns of vegetation with arid geomorphology to refine the projection of dust emissions in global climate change models. This thesis seeks to understand and estimate the impacts of dust emission and transport from the spatial characterization of surface roughness elements.

Arid and semi-arid region land degradation, or desertification, is fundamentally linked to aeolian transport of mineral dust and encroachment and degradation of vegetation. The spatial distribution of surface roughness elements such as vegetation or large rocks may control wind erosion rate and dust emissions and, as a result, arid-region geomorphology. Surface geomorphology is assumed to change from the hypothesis: "dust emissions in the atmosphere are significantly increased by the encroachment of shrubland through changes in the spatial distribution of vegetation, thereby degrading arid deserts". This hypothesis will be tested by two studies: (1) analysis of the pattern of shrub infestation in degraded, aeolian dominated environments, and from (2) the contribution of nonerodible roughness elements distribution in mineral dust flux emissions.

A new geostatistical method presented in Chapter 2 provides a measure of the spatial distribution of vegetation elements in a highly-degraded landscape. In the Jornada del Muerto Basin in New Mexico, shrub encroachment is clearly evident from decreased

intershrub patch size in coppice dunes of 27.8 m relative to shrublands of 65.2 m and grassland spacing of 118.9 m, and a strong SW-NE duneland orientation correlates with the prevailing wind direction and suggests a strong aeolian control of surface geomorphology. In Chapter 3, a new model of aeolian flux incorporating the spatial distribution of vegetation is presented. Shear stress inhomogeneity (m) for vegetated surfaces, was found to have a non-linear relationship with gap size, was reduced with low and high lateral cover ($0.1 < \lambda < 0.3$) and suggests possible wake interference at moderate densities of $\lambda = 0.1$

CONTENTS

List of figures

Acknowledgements

CHAPTER 1

Principles of aeolian erosion and geomorphology in deserts

1. INTRODUCTION

Continentality, anticyclonic subsidence, orographic influences, coastal upwelling of cold water, and the highly reflective albedo of desert surfaces create the major subtropical arid deserts, the majority of which are located between the equator to 30° N, and on the western edge of continents (fig. 1).
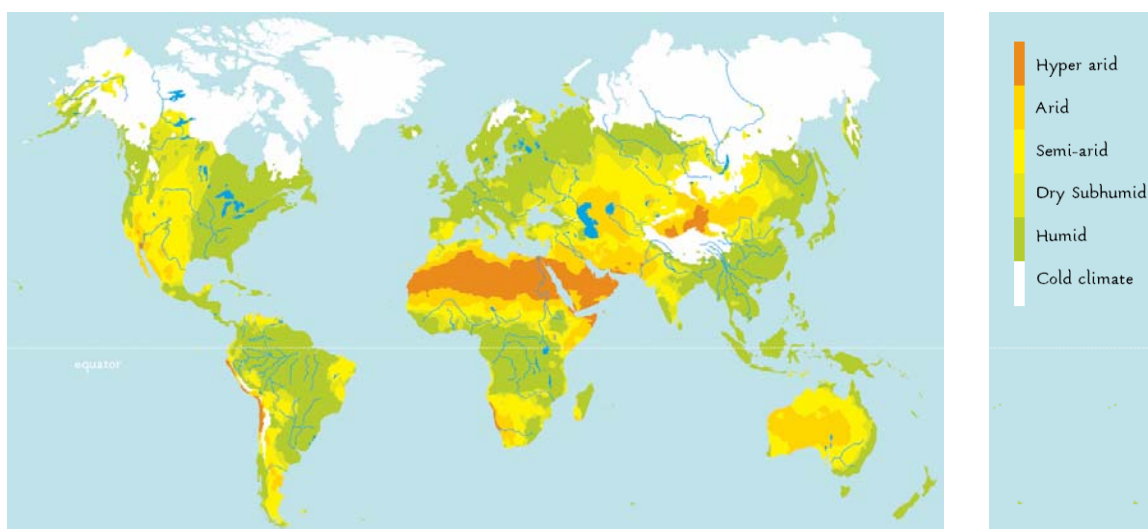
Figure 1. One third of the Earth's land surface is classified as semi-arid to hyper-arid, with deserts formed from anticyclone Hadley-Ferrel cell convergence at 30° N and S latitude, rain shadowing from orographic relief, and distance to moisture (from Houghton et al., 2001).

The deserts of the world are often considered to be barren wastelands incapable of supporting life. They are associated with images of landscapes consisting of extensive sand dunes, dry lakebeds, and limited vegetation. Deserts are highly varied landscapes with robust vegetation and climatic conditions ranging from subhumid to hyperarid. Drylands are found on every continent and cover nearly one-third of the Earth's land surface. Deserts may be defined in various ways, with climate, geomorphology, soils, and

vegetation considered in several definitions (Dregne and Chou, 1992). Generally speaking, though, deserts are defined by a lack of water, which can be measured with indices of aridity, developed as the moisture differential between inputs from precipitation, and outputs from evapotranspiration (fig. 2).
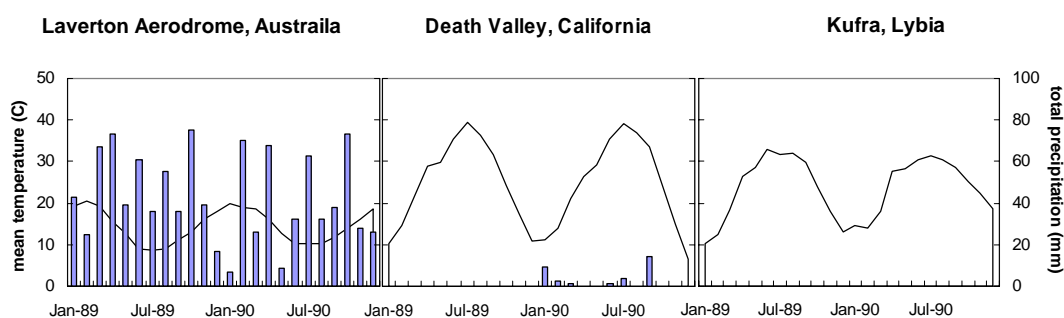
Figure 2. Mean monthly temperature and precipitation records in three arid regions from 1989 to 1990. Laverton Aerodrome in the great Victorian Desert of central Australia consistently receives approximately 40 mm of precipitation each month, with relatively low temperatures from 10 to 20 °C. Death Valley has the hottest recorded temperatures in North America, and is hyper arid with less than 20 mm annual rainfall. Kufra, in the Sahara Desert of Northern Africa is the driest region on Earth, with negligible annual precipitation (National Climate Data Center).

Mineral aerosols, emitted by wind erosion of arid and semiarid areas of the Earth, significantly affect the Earth system. The erodibility of a surface is largely attributed to the surface topography, vegetation cover, and the physical and chemical properties of soils (D'Odorico et al., 2001). The erosion, transport, and deposition of mineral aerosols (herein, dust) by aeolian processes are important environmental processes, and critical indicators of regional environmental conditions. With the potential to impact atmospheric radiative transfer (Sokolik and Toon, 1996), global nutrient cycling (Okin et al., 2004), ocean fertilization (Cotner et al., 1997; Mahowald et al., 2005), cloud formation and precipitation (Wurzler et al., 2000), mineral aerosols produced by dust emission can have a significant effect on the regional and global environment. The processes and patterns determining dust emission and the development of globally-significant dust sources are, however, poorly understood.

2. DUST SOURCES AND GLOBAL IMPORTANCE OF DUST

Deserts are the primary source of mineral aerosols but there are a variety of additional natural sources of aerosols in the atmosphere such as volcanic ejecta, smoke, and sea salt (table 1). Anthropogenic aerosol sources include biomass burning and industrial air pollution (Miller et al., 2004). This thesis will focus on mineral aerosols produced by dust emission from deserts.

2.1. Nutrient cycling

The global biosphere is intricately linked through the chemical weathering, transport and deposition of nutrients. Elements weathered from exposed geologic sources, such as Mg, P, K, and Ca are essential for life. Regions with old, highly weathered soils in humid climates such as oxisols in the Brazilian and Hawaiian rainforest or ultisols and vertisols in Southeast Asia are depleted in mineral-derived nutrients, primarily phosphorus-containing minerals. Although these regions are typically characterized as having high nutrient retention, loss from leaching, fire, and erosion does occur. The loss of mineral derived, biologically available nutrients necessitates foreign inputs to sustain photosynthetic productivity. Mass-balance measurements of nutrient budgets, atmospheric deposition, and isotope analysis of soils have shown that deposition of wind transported nutrients can sustain regions at very large distances from the dust sources (Chadwick et al., 1999). The geographically isolation region of Hawaii supports diverse ecosystems and high productivity due, in part, to the influx of Mg, P, K, and Ca from Asian sources over 6,000 miles to the west. Dust from North African deserts has been attributed as the primary source of P for the P-limited Amazon Basin (Okin et al., 2004;

Swap et al., 1992). The disruption of mineral dust emissions and transport pathways can lead to a systematic degradation of mineral-limited regions globally.

Table 1. Relative estimated contribution of mineral dust to total aerosol emissions (Tg/yr) in 2000 (from Houghton et al., 2001).

	Northern Hemisphere	Southern Hemisphere	Global	Low	High
Carbonaceous aerosols					
Organic matter (0-2 mm)					
Biomass burning	28	26	54	45	80
Fossil fuel	28	0.4	28	10	30
Biogenic (>1 mm)	--	--	56	0	90
Black Carbon (0-2 mm)					
Biomass burning	2.9	2.7	5.7	5	9
Fossil fuel	6.5	0.1	6.6	6	8
Aircraft	0.005	0.0004	0.006		
Industrial Dust (>1 mm)			100	40	130
Sea Salt					
D<1 mm)	23	31	54	18	100
D=1-16 mm)	1420	1870	3290	1000	6000
Total	1440	1900	3340	1000	6000
Mineral Dust					
D<1 mm)	90	17	110	--	--
D=1-2 mm)	240	50	290	--	--
D=2-20 mm)	1470	282	1750	--	--
Total	1800	349	2150	1000	3000

Aeolian dust deposits are also a significant source of mineral-derived nutrients in ocean environments. Large amounts of terrestrial-sourced dust particles are deposited in the oceans (fig. 3). Wind-transported Fe, N, and P inputs are common, but only Fe and P are readily soluble and easily accessible by microorganisms (Baker et al., 2006). Several studies have suggested a restriction of microbial activity from phosphorous limitations in the Atlantic and Indian oceans (Cotner et al., 1997; Sanudo-Wilhelmy et al., 2001), and strong response of microbial biomass increase to iron sediments from large dust events in the Pacific (Bishop et al., 2002; Mahowald et al., 2005).

2.2. Radiative transfer

Incoming solar radiation drives the climate and most life on the planet. Aerosols in the atmosphere can scatter and absorb solar radiation (Li et al., 1996), and have both direct and indirect effects on climate. Direct effects result from the scattering or

absorption of radiation by aerosols in the atmosphere (fig. 4). Indirect effects result from the impact of aerosols on cloud-forming processes, resulting in changes in cloud cover that impact the radiation budget.

The direct effect of desert dust on global or regional climate is complex, because dust can either scatter incoming short-wave solar radiation back to space or absorb infrared light. Thus, the presence of dust in the atmosphere can result in a net negative or net positive radiative forcing (Sokolik and Toon, 1996; Tegen et al., 1997). Negative forcing due to increases in atmospheric albedo from the presence of scattering aerosols is expected to be strongest over low-albedo regions such as oceans. Positive forcing, due to absorption of incoming shortwave or outgoing longwave radiation is typical in desert environments and other high-albedo surfaces such as snow, providing a strong thermal contrast between continents and oceans. The presence of mineral dust has been shown to reduce photolysis rates throughout the atmosphere (Liao et al., 1999).
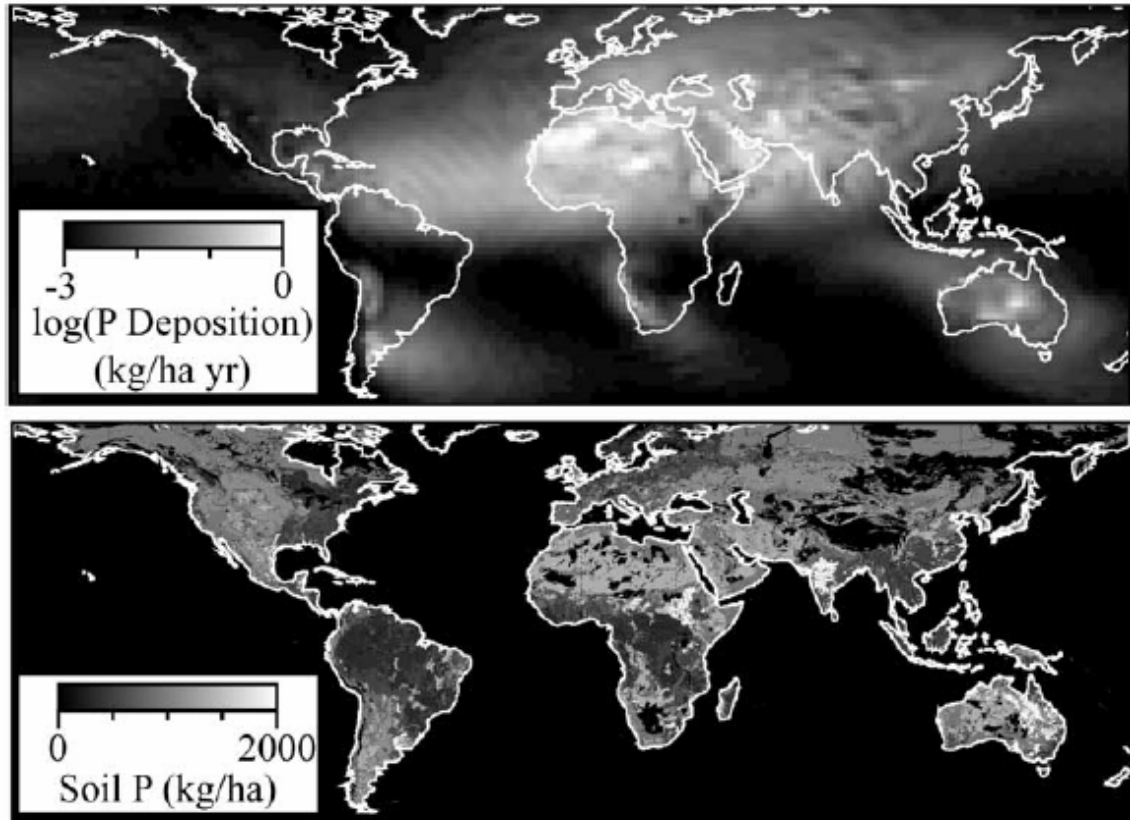
Figure 3. Large-scale transport of and deposition from Saharan and central-Asian sourced P as mineral dust provides a substantial influx to highly depleted P regions in the Amazon basin, central Africa, and southeast Asia (from Okin et al., 2004).

African dust has been observed to be the predominant light-scattering aerosol over the North Atlantic (Li et al., 1996). With a global climate model, Tegen et al. (1996) suggested mineral aerosols create a negative global mean forcing at the surface of 1 W m^{-2}. More recent studies of direct radiative forcing have suggested a larger global decrease of 1.9 W m^{-2} (Bellouin et al., 2005), and local radiative transfer models predicting 4.7 W m^{-2} (Liao and Seinfeld, 1998).

In the presence of a cloud layer, radiative forcing by mineral aerosols is sensitive to altitude (Haywood and Boucher, 2000). When atmospheric dust is above a cloud layer, incoming solar radiation and reflected radiation from the clouds are absorbed, warming the upper atmosphere from 3.5 to 5.0 W m^{-2} over low to high albedo surfaces, and

negative forcing of -1.5 to -0.8 W m^{-2}. Dust below a cloud layer increases multiple scattering with a lower radiative forcing in the upper atmosphere -0.2 to 2.0 W m^{-2} and higher negative forcing on the surface -1.6 to -1.4 W m^{-2} (Liao and Seinfeld, 1998).

The indirect effects of mineral aserosols on atmospheric radiative transfer are not yet fully understood. Clouds are the most important, and most variable, controls on total planetary albedo. Mineral aerosols impact cloud formation because dust particles can behave as cloud condensation nuclei (CCN) (Warner and Twomey, 1967). Thus, the presence of dust can increase cloud cover, and hence albedo, while reducing precipitation (Rosenfeld et al., 2001; Warner and Twomey, 1967). Suppression of precipitation has been suggested to occur as the result in decreases in cloud droplet size related to increases in CCN concentration. When atmospheric dust is above a cloud layer, incoming solar radiation and reflected radiation from the clouds are absorbed, warming the upper atmosphere from 3.5 to 5.0 W m^{-2} over low to high albedo surfaces, and negative forcing of -1.5 to -0.8 W m^{-2}. Dust below a cloud layer increases multiple scattering with a lower radiative forcing in the upper atmosphere -0.2 to 2.0 W m^{-2} and higher negative forcing on the surface -1.6 to -1.4 W m^{-2} (Liao and Seinfeld, 1998).

The intricate feedback of both positive and negative radiative forcing and high uncertainty of predictions of future dust emissions hinders definitive assessment of how mineral aerosols impact atmospheric radiative transfer. Preliminary estimates from the Intergovernmental Panel on Climate Change (IPCC) science report predicted a net global increase of dust emissions by 10% in 2100, but with high regional and spatial variability (Houghton et al., 2001). Saharan dust refractive index measurements were inferred to estimate a small net increase in radiative forcing globally. Up to 50% of mineral dust

emissions were attributed to anthropogenic land use changes. Past natural dust emissions were assumed to be constant. Both assumptions are highly speculative and omit natural variations in vegetation, climate, and atmospheric circulation which certainly have not remained constant, and should contribute to high variability in dust emissions, as has been reported for the past century (Prospero and Lamb, 2003). Accurate quantification of dust sources and predictions of future spatial and temporal variability of emissions is essential for substantial progress in climate change models.

(A)

(B)
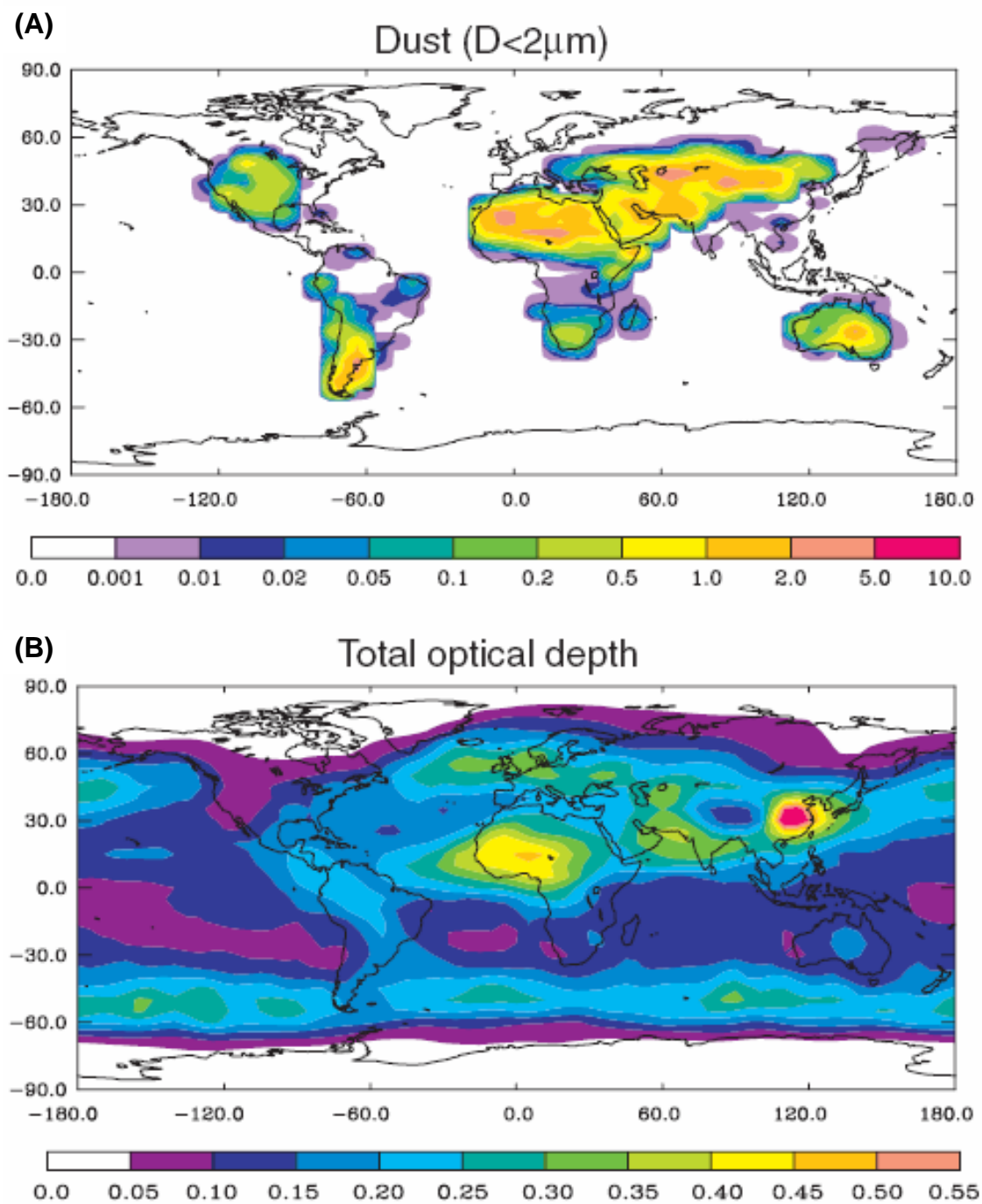
Figure 4. Global distribution of dust emissions, concentrated in Northern Africa and Central Asia (A), corresponding with dust transport concentrated in Western Africa (B) (from Houghton et al., 2001).

3. AEOLIAN PROCESSES RELATED TO PRODUCTION OF MINERAL AEROSOLS

The largest dust sources in the world are in hyperarid areas and drylakes. Dust emissions can also originate from semiarid areas, particularly when the vegetation is degraded or the surface is disturbed by anthropogenic activities. Desert dust generally consists of sediment and soil particles with diameters from $\sim$ 2 to 50 μm (Pye, 1987), although only the smallest particles (< 10 μm) are transported long distances. Particles are transported by wind through saltation, creep and suspension.

3.1.   Law of the wall and friction velocity

Many attempts have been made to model desert dust emissions. Dust emission models have been generally based on the observation that wind erosion and dust emission are initiated when a minimum wind velocity threshold has been reached, and are not linearly dependent upon wind velocity (Bagnold, 1941). At distances approaching a surface, viscous flow dominates, creating a boundary layer with no pressure gradient. The velocity profile near that surface approaches zero. Particle flux near the surface is controlled not by the wind velocity, but by the roughness characteristics of the surface, and the associated boundary layer thickness. Movement at the surface is characterized by a relationship of shear stress (τ_0) and air density (ρ), known as friction velocity (u_*).

$$u_* \equiv \sqrt{\frac{\tau_0}{\rho}} \tag{1}$$

This can also be expressed with the law of the wall, where velocity and friction velocity are a function and where $\frac{y u_*}{v}$, y is a nondimensionalized distance.

$$\frac{U}{u_*} = f\left(\frac{yu_*}{v}\right) = f(y) \tag{2}$$

For rough, natural surfaces, roughness elements must be introduced which disturb the movement between the viscous sublayer and outer layer. The geometry of rough elements on the surface create a pressure drag and modify the law of the wall to account for roughness height, y_0 and the von Karman constant (k) in turbulent flow.

$$\frac{U}{u_*} = \frac{1}{k}\ln\left(\frac{y}{y_0}\right) \tag{3}$$

In high density vegetated surfaces, the boundary profile becomes distorted near the surface, which can be corrected as the difference between the height y and with the introduction of mean momentum displacement d.

$$\frac{U}{u_*} = \frac{1}{k}\ln\left(\frac{y-d}{y_0}\right) \tag{4}$$

A series of papers by Raupach (Raupach, 1991; Raupach, 1992; Raupach, 1994; Raupach et al., 1993) presented a modification of roughness characteristics on saltating surface to increase the roughness length. In areas of little or sparse vegetation, the roughness sublayer below the mean momentum sink can be difficult to quantify but creates critical sheltered areas from downwind wake effects which limit the predictive erodibilty of some surfaces.

3.2.   Wind threshold friction velocity

Several equations to predict horizontal aeolian flux have been suggested. One such model is (Gillette et al., 1996):

$$q(x) = f(x)A\frac{\rho}{g}u_*(u_*^2 - u_{*_t}^2) \tag{5}$$

where, q is the horizontal sediment flux (g/m s⁻1), A is a dimensionless constant, ρ is the density of air, g is gravitational acceleration, u_* is friction velocity, u_{*_t} is threshold friction velocity. Once a particle movement has been initiated by overcoming the threshold friction velocity, it often looses velocity and impacts into the surface. This collision initiates the movement of disrupted surface particles from the impact, increasing horizontal flux and creating an avalanche effect, similar to the propagation of downslope snow movement. The saltation movement of particles along the surface increases the aerodynamic roughness height. An internal boundary layer is formed from the increase in surface roughness, creating a positive feedback system where both flux and roughness can increase.

3.3. Sandblasting

Particle movement from saltation and sandblasting are the primary mechanism of dust entrainment. Through the net horizontal movement of saltation, surface particles are entrained by aerodynamic forces through a series of ballistic jumps on a centimeter scale within the near-surface turbulent layer. Through sandblasting, particles can be entrained at u_* lower than soil saltation thresholds, transporting large particles and dust (Alfaro and Gomes, 2001; Gomes et al., 1990). With each ballistic impact, kinetic energy and momentum is transferred from impacting particles, and can break cohesive interparticle bonds on the surface, releasing tightly-bonded, fine-grained desert dust (Shao et al., 1993).

3.4. Grain size

The initiation of aeolian transport can occur at the minimum friction velocity, the threshold friction velocity ($u_* = u_{*_t}$). This initiation is when such as those due to

mineralogy, soil moisture, and microbial crusts, are less than the driving forces of aerodynamic drag (F_d) and lift (F_l). For dry and bare surfaces, typical of arid and semi-arid regions, Shao and Lu (2000 suggest a threshold equation modified from Greeley and Iversen (1985), where A_N is an experimental value for u_{*t} and particle diameter derived

$$u_{*t} = \sqrt{A_N \left(\sigma_p gd + \frac{\gamma}{\rho d} \right)} \qquad (6)$$

from the particle friction Reynolds number where $A_N \simeq$ 0.11-0.12 for $d >$200 μm, σ_p is the particle to air density ratio, d is particle size, and γ results from a curve fit. Wind tunnel results give recommended values of $A_N = 0.0123$, $\gamma = 3 \times 10^{-4}$ kg s^{-2}, assuming spherical particles. Threshold friction velocity for a variety of diameters were shown by Marticorena and Bergametti (1995) in figure 5.
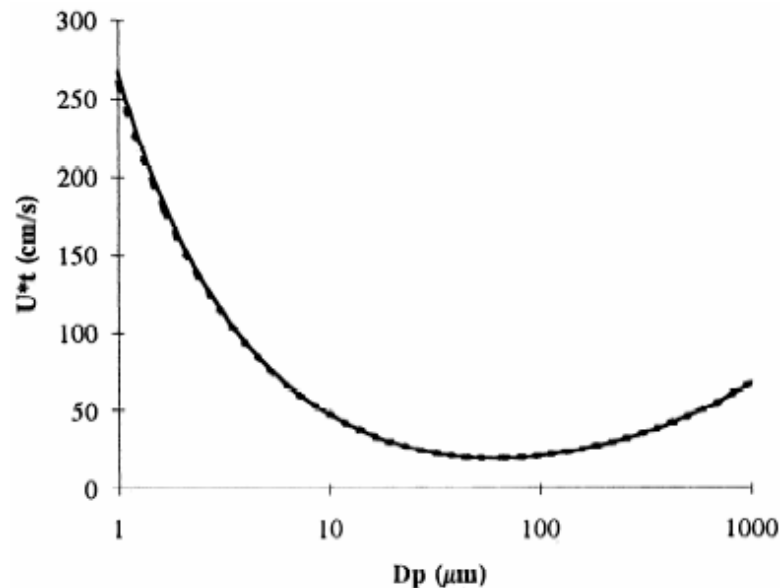
Figure 5. Threshold friction velocity for a variety of particle diameters (from Marticorena and Bergametti 1995).

Physical characteristics such as the size distribution of loose particles and atmospheric characteristics such as surface roughness are primary factors controlling the

aeolian erosion of surfaces. Bagnold (1941) and Marticorena and Bergametti (1995) investigated the erosion threshold and erosion strength with surface roughness and wind friction velocity.

$$q = f\left(u_*, u_{*_t}\right) \text{ g cm}^{-1} \text{ s}^{-1} \tag{7}$$

While soil moisture and organic matter is not included, application of the model determined emission production rates for a variety of soil ranges and surface types. Soil size distribution, roughness length, and wind friction velocity were all considered to be primary parameters. Analytical values for the various mechanisms acting upon soil erosion previously mentioned were calculated. Suspension was found to act on particles of sizes < 60 μm. Saltation occurs for particles from 60-2000 μm, where initiation of movement can occur, but lift is insufficient to sustain transport. Larger particles (> 2000 μm) become too heavy for vertical movement and instead move along the surface, a phenomenon known as creeping.

3.5.   Soil moisture

Moist or wet soils have long been observed to experience little or no entrainment of dust particles, relative to comparable dry surfaces, even when wind threshold velocities are exceeded. Soil moisture creates interparticle bonds between surface grains reducing the erosive potential. Capillary bonds in equilibrium with the atmosphere, create a pressure differential between pore water particles and the air (Cornelis and Gabriels, 2003). Individual particles are also coated with a moist microlayer formed from a polarized bond between charged particles called the electrostatic force (Ravi et al., in press). Water may also act as an absorptive buffer, diminishing the momentum and kinetic energy transfer to surface particles during bombardment. These cohesive forces

are likely to be in a constant state of disequilibrium, due to natural variability in surface soil moisture via ambient humidity (Ravi and D'Odorico, 2005; Ravi et al., 2004).

4. EFFECT OF VEGETATION ON DUST EMISSIONS

The structure and spatial arrangement of vegetation modulates aeolian emission and transport, and thus plays a pivotal relationship in controlling arid-region geomorphology. Vegetation can have a strong influence on wind erosion rates and wind erosion thresholds. While vegetation is associated with surface roughness, zero plane displacement and boundary layer turbulence, the placement and distribution of vegetation calls for increased scrutiny (Poggi et al., 2004). Vegetation present in arid regions resists the erosion of soil, inhibits deflation, reduces surface velocity and provides sites for deposition (Wolfe and Nickling, 1993).

As a driving factor of land degradation, soil erosion by wind is dependent upon roughness properties of the surface. Threshold friction velocity ratio (R_t), is the ratio of the threshold friction velocity of erodible soil without roughness to that of a soil with nonerodible roughness. Raupach et al. (1993) created a model for R_t, based on the partitioning of shear stress between the vegetation and the soil surface:

$$R_t = (1 - m\sigma\lambda)^{-1/2}(1 + m\beta\lambda)^{-1/2} \tag{8}$$

where $m < 1$ accounts for the stress difference from the substrate surface stress and the maximum stress on the surface at a point, σ is the area ratio of the roughness element, λ is the roughness density, and β is the ratio of the drag coefficient from a single, isolated surface roughness element to the coefficient of drag for the substrate surface.

The first term $(1-m\sigma\lambda)^{-1/2}$ is the increase in stress on erodible surfaces and $(1+m\beta\lambda)^{-1/2}$ represents the decrease in stress in the shadowed area created by nonerodible elements. Defined in terms of threshold friction velocity for vegetated surfaces gives:

$$u_{*_{tv}} = u_{*_{ts}}\sqrt{(1-m\sigma\lambda)(1+m\beta\lambda)} \qquad (9)$$

where $\beta = 100$, $m = 0.5$ for erodible surfaces of bare soil, and $m = 1.0$ for highly stable surfaces. Nonuniform surface stress only affects the second parameter under the radical $(1+m\beta\lambda)^{-1/2}$, where typically $(1-m\sigma\lambda)^{-1/2}$ is unaffected in low densities of $\lambda \ll 1$.

5. INTEGRATION OF REMOTE SENSING ANALYSES

Remote sensing data products provide direct information on surface features and offer a range of scales from which to view synoptic features. Remote sensing also affords the best opportunity to study aeolian transport processes and geomorphology in harsh conditions, assess environmental change over long periods, and on large scales infeasible through traditional field-based methods. Remote sensing is a powerful tool for observing the Earth's surface and atmosphere. Most remote sensing studies of dust have focused on dust in the atmosphere. A second class of studies has monitored and analyzed surfaces features related to dust emissions.

5.1. Direct detection of airborne dust

Suspended dust in the atmosphere can be directly measured by an increasing range of multispectral, hyperspectral, and multiangle active and passive instruments (King et al., 1999). Solar radiation, reflected from the Earth's surface is scattered and

absorbed by atmospheric constituents allowing for reliable measurements of mineral dust aerosols, in addition to biogenic and anthropogenic sources. Platforms such as the TOMS (Total Ozone Mapping Spectrometer) instrument with dual-channel UV sensors are ideally suited to extract abundance in the atmosphere (Diaz et al., 2001; Torres et al., 2002). Other platforms enable estimates of aerosol concentrations calculated from the atmospheric optical thickness, aerosol size distributions, and scattering albedo, which have been integrated into processed multispectral products (Satheesh et al., 2006; Tanre et al., 1997). Common multispectral instruments such as MODIS (Moderate-resolution Imaging Spectroradiometer) and AVHRR (Advanced Very High-Resolution Radiometer) have had some success measuring aerosol retrieval from observed radiance to optical depth (Husar et al., 1997; Karyampudi et al., 1999; Sokolik and Toon, 1999) but make several assumptions on scattering dispersion patterns by aerosol constituents. Multiangle instruments provide specific enhancements to measure aerosols, not viable with traditional nidar instruments. Indirect (non-nidar) viewing angles enhance aerosol signals from longer atmospheric path lengths. Aerosols of different compositions can also be extracted from surface reflectance by anisotropic scattering at different angles (Diner et al., 1999; Kaufman et al., 2002). Unfortunately, difficulties in spectral extraction of aerosols between highly-reflective continents, and dark oceans persist, regardless of instruments and methods. Aerosols-associated atmospheric features such as cloud development and formation, and radiative forcing are also feasible. Geomorphic evidence of aeolian transport, including dune mobility (Bullard, 1997) and aeolian deposition (Farr and Chadwick, 1996) have also been examined using remote sensing.

5.2. Indirect assessment of dust mobilization from land surfaces properties

Studies that have used remote sensing to characterize the surface features that directly control wind erosion are much less common than remote sensing studies of dust once it is already aloft. However, remote sensing can provide information about surface features that are associated with wind erosion and dust emission. Vegetation for example, can be characterized by vegetation indices (e.g., EVI, LAI, NDVI), spectral-mixture analyses (Okin et al., 2001b; Rango et al., 2000), and LIDAR (Rango et al., 2000).

Predicting future dust emissions with climate changes requires more detailed understanding of global dust emissions, transport, and loading from large-scale studies of sites with varying landcover. Adaptive vegetation measures must be developed to achieve more accurate land cover characterization. Current classifications often focus on pixel-based vegetation indexes such as NDVI, which are optimized for moist temperate regions and perform poorly in the highly reflective environment with low vegetation cover, typical of arid regions (Baret and Guyot, 1991; Huete et al., 2002). A utilization of multispectral, multitemporal, and multiplatform data can enhance classifications of dryland regions that provide information about surface conditions directly related to aeolian transport.

6. STRUCTURE OF THE THESIS

Arid and semi-arid region land degradation is fundamentally linked to aeolian transport and vegetation. However, the highly variable nature of vegetation makes it difficult to characterize the precise relationship between the two. The spatial distribution of vegetation may be a fundamental component of dust emissions as nonreodible roughness elements and the association with aeolian erosion and resource availability.

Two studies will examine spatial components of vegetation cover and associated dust emissions from the perspective of aeolian geomorphology. Geostatistical calculations on remotely sensed datasets will be applied to specifically examine two aspects of arid geomorphology: 1) the pattern of shrub infestation in degraded, aeolian dominated environments, and 2) the contribution of nonerodible roughness elements distribution in mineral dust flux emissions. A new geostatistical method presented in Chapter 2 provides a measure of the spatial distribution of vegetation elements in a highly-degraded landscape. In Chapter 3, an analysis of roughness elements is performed to demonstrate the importance of spatial relationships of vegetation with dust emissions. A new model of aeolian flux incorporating the spatial distribution of vegetation is presented.

CHAPTER 2

Characterization of shrub distribution using high spatial resolution remote sensing: Ecosystem implications for a former Chihuahuan Desert grassland

(This chapter is in Remote Sensing of Environment, 101 (2006) 554-566.)

Abstract

Patchiness is often considered a defining quality of ecosystems in arid and semiarid regions. The spatial distribution of vegetation patches and soil nutrients coupled with wind and water erosion as well as biotic processes are believed to have an influence on land degradation. A geostatistical measure of spatial "connectivity" is presented to directly measure the size of patches in the landscape from a raster dataset. Connectivity is defined as the probability that adjacent pixels belong to the same type of patch. Connectivity allows the size distribution of erodible patches to be quantified from a remote sensing image or field measurement, or specified for the purposes of modeling.

Applied to high-resolution remote sensing imagery in the Jornada del Muerto Basin in New Mexico, the spatial distribution of plants indicates the current state of grassland-to-shrubland transition in addition to processes of degradation in this former grassland. Shrub encroachment is clearly evident from decreased intershrub patch size in coppice dunes of 27.8 m relative to shrublands of 65.2 m and grassland spacing of 118.9 m. Shrub patches remain a consistent 2-4 m diameter regardless of the development of bush encroachment. A strong SW-NE duneland orientation correlates with the prevailing wind direction and suggests a strong aeolian control of surface geomorphology.

With appropriate datasets and classification, potential applications of the connectivity method extend beyond vegetation dynamics, including mineralogy mapping, preserve planning, habitat fragmentation, pore spacing in surface hydrology, and microbial community dynamics.

1. INTRODUCTION

Shrub encroachment is a global phenomenon documented in arid and semi-arid regions of Africa, Australia, and North America (Archer, 1995; Fensham et al., 2005; Roques et al., 2001). In the Chihuahuan Desert grasslands of North America, shrub encroachment has been especially pronounced, with significant transformation of vegetation community structure occurring in the last 150 years. Populations of grasses, primarily black grama (*Bouteloua eriopoda*) once dominated 90% of the region but have diminished to less than 25% (Buffington and Herbel, 1965; Gibbens et al., 2005). Drought-resistant shrub cover, primarily comprised of creosote (*Larrea tridentata*) and mesquite (*Prosopis glandulosa*), has increased by a factor of 10 over the same period, replacing the native grasses (Gibbens et al., 2005; Rango et al., 2000; Reynolds et al., 1999). Causes of shrub encroachment and grassland deterioration such as rainfall variability, elevated CO_2, changes in fire regime, seed dispersal and livestock grazing have been suggested (Archer, 1995; Scanlon et al., 2005), but the definitive cause of the transformation remains unknown (Archer, 1995; Bahre and Shelton, 1993; Dougill and Thomas, 2004).

The change in the spatial distribution of vegetation is an important aspect of shrub invasion. Shrubs create "islands of fertility" by trapping soil resources beneath their canopies (Schlesinger et al., 1990; Whitford, 1992). The transition from grass to shrub cover increases the scale of spatial heterogeneity and the dominant small-scale processes can be reflected through the position of individual plants (Schlesinger and Pilmanis, 1998). Thus, the ability to quantify the spatial distribution of plants could indicate the current state of transition in addition to processes of degradation in semiarid mixed-shrub grasslands.

Remote sensing provides an opportunity to monitor and understand spatial patterns of vegetation and to inform the understanding of biotic and abiotic processes related to those patterns. The physical and spectral properties associated with vegetation cover and surface morphologic structures observed by remote sensing are being continuously refined (Bradley and Mustard, 2005; Okin and Painter, 2004; Okin et al., 2001b; Weeks et al., 1996) especially with the incorporation of spatial patterns of vegetation (Caylor et al., 2004; Okin and Gillette, 2001; Privette et al., 2004; Scholes et al., 2004).

High spatial resolution remote sensing enables direct imaging of plant individuals that are at least the size of the ground resolution of the remote sensing image. This capability makes possible demographic studies of vegetation such as Schlesinger and Gramenopoulos's (1996) use of archival photographs to show that there were not climate-induced changes in woody vegetation in the Sudan from 1943 to 1994, and with individual-based monitoring of vegetation change in the Jornada Basin (Rango et al., 2002).

The ability to image individual plants with high resolution remote sensing opens up the possibility of effective use of geostatistical methods for describing the distribution of plants. Phinn et al., (1996) and Okin and Gillette (2001) have shown that traditional variograms can provide an accurate measure of average plant spacing in shrublands of the Chihuahuan Desert. Nonetheless, variograms provide limited information about the landscape. In particular, because variograms are calculated on the basis of pairs of data separated by some distance (lag), this method cannot provide information about conditions between these pairs. In landscapes where the connectedness of soil or vegetation patches (providing conduits for wind, water, seeds, small mammals, etc.) is important, a different geostatistical metric of two-dimensional landscape structure is advisable.

A new application of geostatistical techniques is presented to evaluate the connectivity of plant and soil patches. This connectivity function calculates the probability that contiguous pixels belong to the same class, or in this application, the probability that contiguous pixels are or are not occupied by shrubs.

In this study, we present the use of connectivity to provide spatial information about patch size and anisotropy and show that the results are robust for patchy landscapes. Using an object-oriented classification on digitized orthophotos of our field site in New Mexico, individual 1 m pixels are separated into shrub and not-shrub classes. We then apply the connectivity statistic to the classified images to characterize the spatial nature of shrub encroachment and the spatial characterization of individual shrub patches. As a geostatistical measure, the use of connectivity is independent of the choice of classification scheme. The progressive nature of shrub encroachment is evaluated through

the comparison of shrub and intershrub patch characteristics amongst differing areas of establishment. Specifically, we present the theory and definition of connectivity geostatistics, provide validation of connectivity based on stochastic simulation, and demonstrate the utility of connectivity using a case study to examine the variability of spatial distribution of vegetation in the Jornada Basin of New Mexico.

2. MATERIAL AND EXPERIMENTAL METHODS

2.1. Connectivity

We used a geostatistical measure of the connectedness of patches in the landscape called "connectivity." For a raster dataset, connectivity is defined as:

$$C(\vec{h}) = \frac{1}{n} \sum_n \left(\prod_{\vec{h}} I_i \right) \tag{1}$$

where C is the connectivity, $\vec{h}$ is the lag vector with length $|h|$, n is the number of consecutive sets of pixels along $\vec{h}$ in an image, and I_i is an indicator variable equal to 1 for pixels that belong to the class of interest and 0 otherwise. The connectivity at $\vec{h}=0$ is denoted as C_o and is equal to the fraction of pixels in an image that belong to the class of interest. For example, if "shrub" is the class of interest, then pixels that are classified as "shrub" are given a value of 1, and all other pixels are given a value of 0. In this case, C_o will be equal to the fraction of pixels that are classified as "shrub", or in other words, the fractional shrub cover.

Connectivity may also be interpreted as a probability. In the case of C_o, the connectivity is the probability that any pixel in an image belongs to the class of interest. $C(\vec{h})$ is the probability that any set of consecutive pixels along $\vec{h}$ all belong to the class

of interest (fig. 1). When interpreted as probabilities, it is intuitive that connectivity always decreases with increasing lag distance, $|h|$.

In practice, the decrease in connectivity with $|h|$ approximates an exponential decay function (fig. 2). Thus, to derive a single statistic for the spatial scale of landscape connectedness similar to the "range" in traditional variograms, we modeled connectivity as:

$$C(\vec{h}) = C_o \exp\left(-\frac{|\vec{h}|}{\alpha}\right) \tag{2}$$

From Equation (2), it is clear that the range (α) is an e-folding distance at which the connectivity drops to C_o/e.
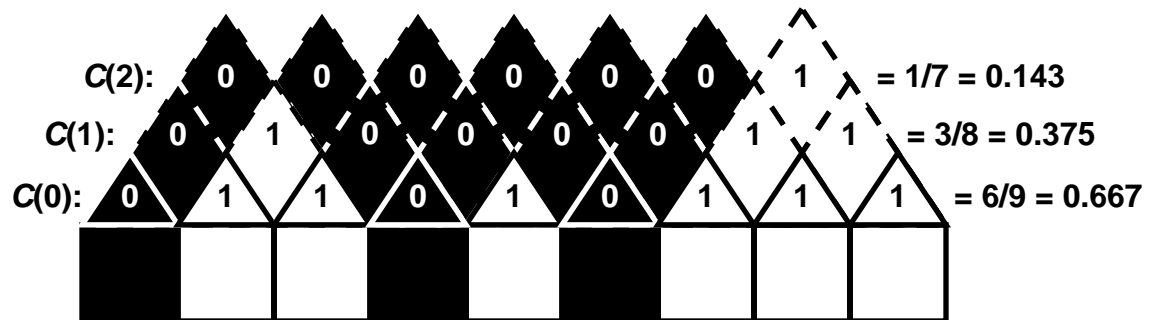
Figure 1. Connectivity is calculated on the number of consecutive sets of pixels in an image, as 1 for pixels that belong to the class of interest and 0 otherwise with increasing lag distance, as demonstrated for 1, 2, and 3 pixel distances.

Lag is treated as a vector $\vec{h}$, allowing for connectivity to be calculated along any azimuth in an image, and α can be determined as a function of azimuth angle. In this study, the resulting polar plots of azimuth and range were smoothed using a low pass fast Fourier transform filter. Geometric properties were derived from the curves such as orientation, the preferential azimuth, and elongation (fig 3). Elongation is defined as:

$$\text{elongation} = \frac{\alpha_{max}}{\perp \alpha_{max}} \tag{3}$$

the ratio of the maximum range (α_{max}) and the range perpendicular to the maximum

azimuth, $\alpha(\perp\alpha_{max})$.

The integration of continuously similar or connected values has been presented in broad applications of geospatial components. Investigations into water transport include spatial connectivity of river channels (Krishnan and Journel, 2003) fractured rocks with three-dimensional percolation from small- to large-scale fault networks(Bour and Davy, 1998), the spatial density of connectivity of fracture networks in rocks with interest in water transport (Renshaw, 1999), and homogenous soil moisture patterns (Western et al., 1998). Incorporation of our connectivity statistic may expand the usage of multiple-point spatial distributions in hydrogeology and throughout the environmental sciences.
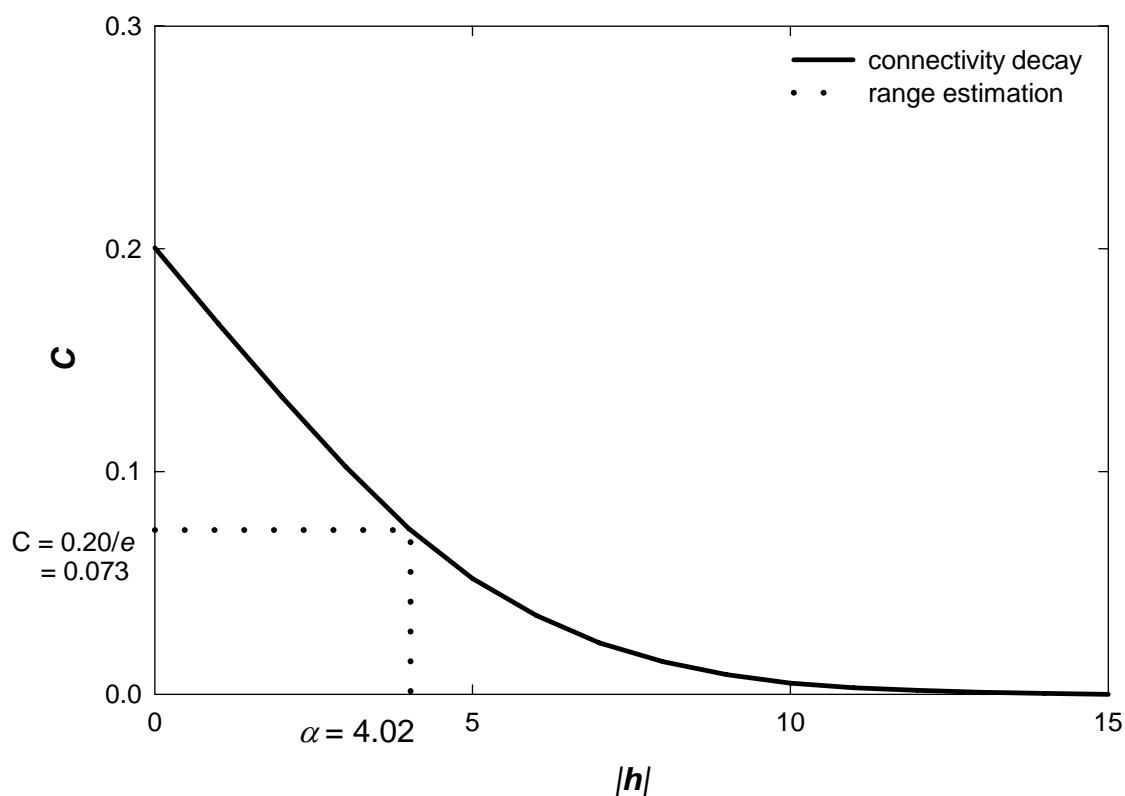
Figure 2. Representative connectivity curve for 20% cover, a range of 4.02 (dashed line) and generally approximates an exponential decay curve.

2.2.   Connectivity simulations

To verify that connectivity provides a robust representation of spatial patterns in remote sensing imagery, a series of tests were performed on simulated images created using the geostatistical software package GSLib (Deutsch and Journel, 1998). The simulated images were generated using the unconditional simulated annealing algorithm with variogram constraints.
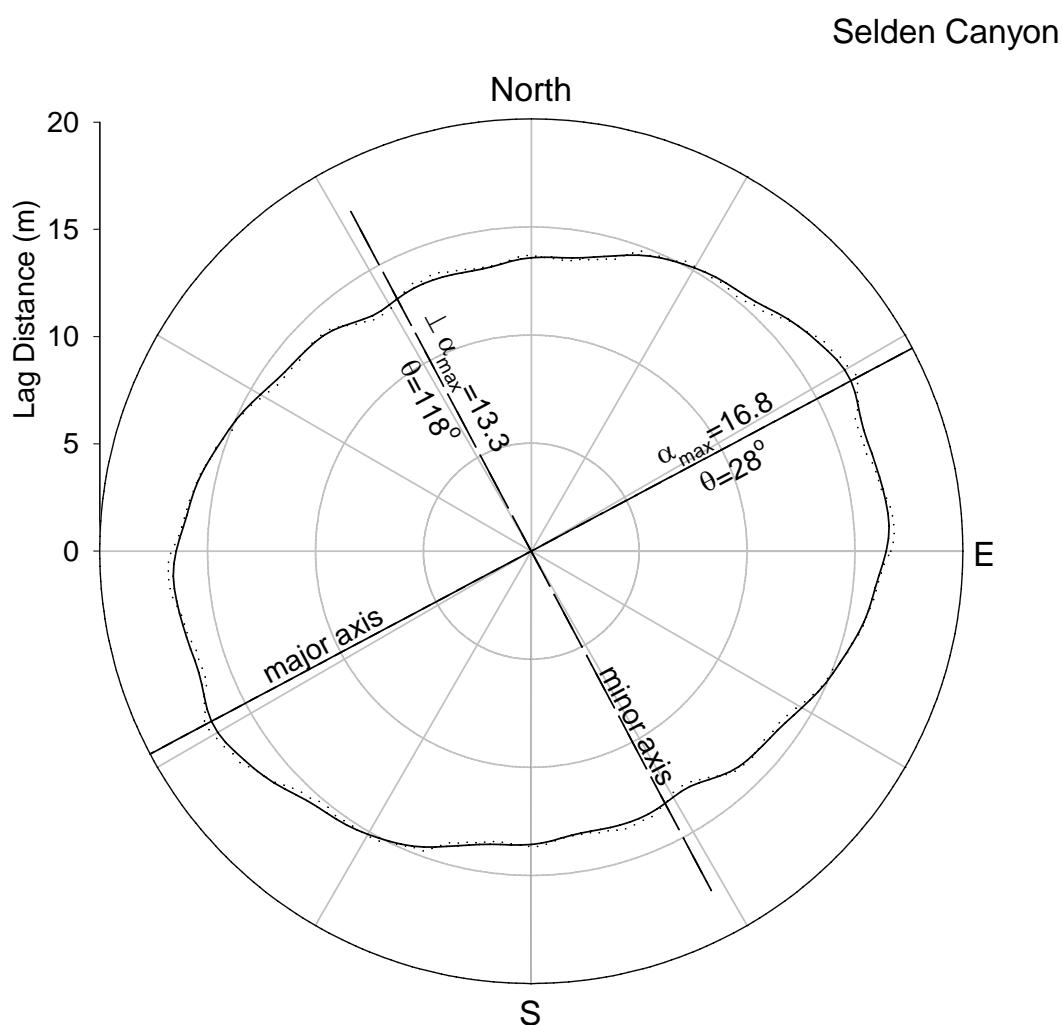
Figure 3. Polar plot of elongation values (dotted line) smoothed with a Fast- Fourier Transform (FFT) (solid line) and dominant orientation direction from the major axis.

In one test, normalized anisotropic Gaussian variograms (sill=1, nugget=0) were utilized, with the major axis having a range of 10 and the minor axis having a range of 6. Nineteen sets of 200 x 200 pixel images were generated using this variogram model with the direction of the major axis varying from 0 to 180° at 10° intervals, with an additional duplicate at 90° (fig. 4). Three stochastic simulations were produced at each angle interval. This resulted in a total of 57 8-bit images with values between 0 and 99. A 3x3 mean pixel filter was applied to remove individual isolated pixels and fill patches to more accurately mimic the solid clumps observed in natural settings, and a threshold was chosen to convert the image into a binary classification. Connectivity calculations were then performed individually on each of the 57 images.
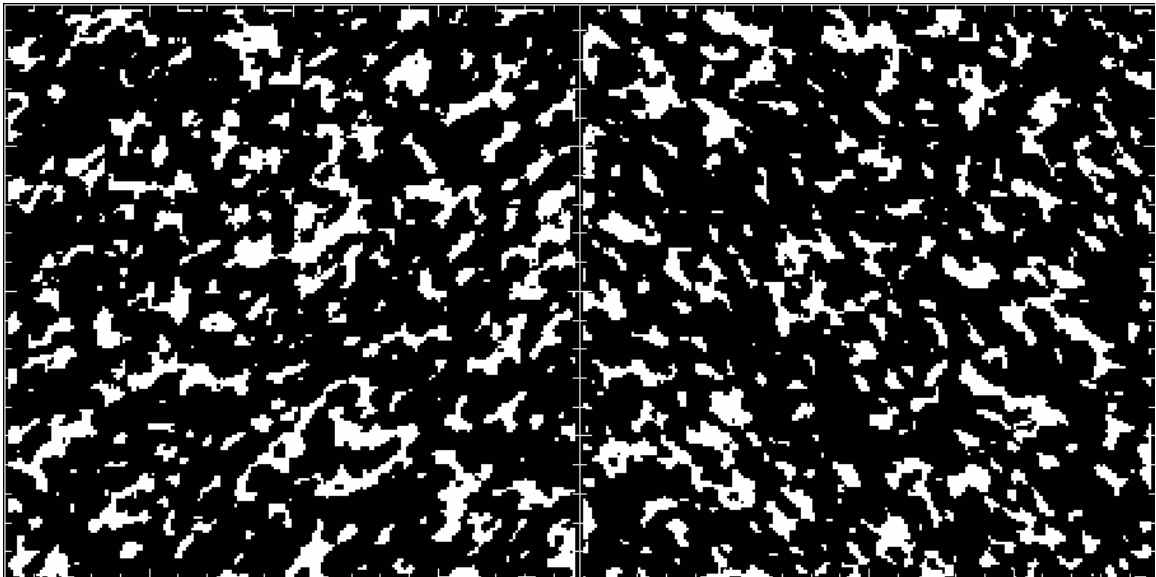
Figure 4. Simulated images at 40° and 140° orientation with 20% cover used for testing connectivity orientation angle.

In a second test, the relation between variogram range and connectivity was explored by the generation of 11 sets of 200 x 200 pixel isotropic images with range

values from 1 to 20 pixels and one set at 40 pixels using the same variogram model (fig. 5). The simulated images provided a direct analysis of the dependence of connectivity on patch size. A 3x3 mean pixel filter was then applied to the resulting 33 8-bit images with values between 0 and 99. For each image the cumulative distribution function (CDF) was calculated, allowing the creation of images with a specified fraction of each image below a specific threshold determined from the CDF. These images mimic in appearance orthophotos classified into shrub and not-shrub classes, with the scale of shrub patches defined by the range of the variogram used to in the simulation. Connectivity range calculations were performed on images with simulated cover varying from 10% to 90% in 10% increments. The mean connectivity range of three realizations with each variogram range and fractional cover are reported.
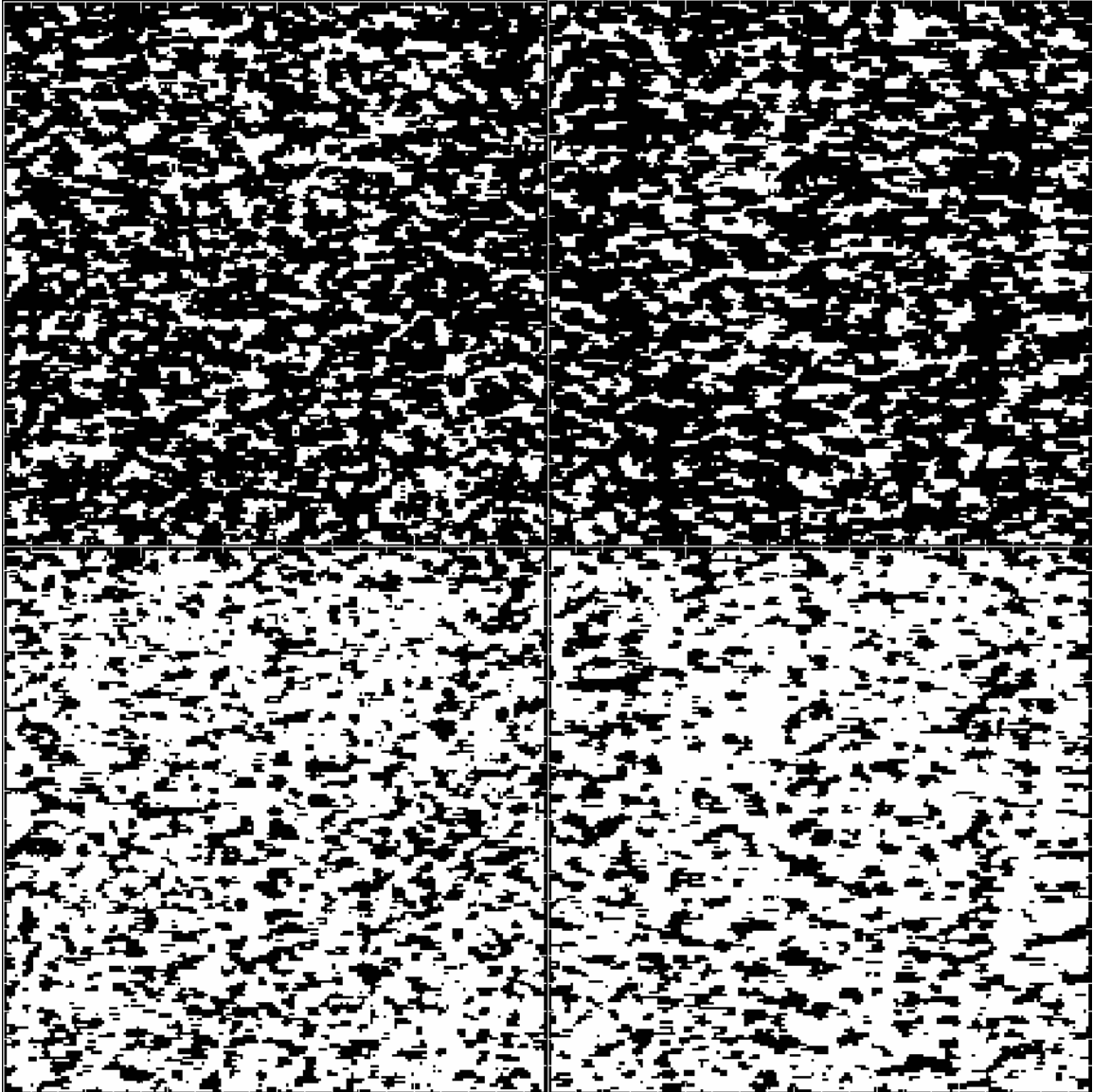
Figure 5. Simulated images at 0° orientation with 30% (top) and 70% (bottom) cover and a controlled range of 5 (left) and 10 (right) pixels.

2.3.   Study area

The connectivity method provides a quantitative method to measure the vegetation characteristics in different landscapes. Connectivity was tested on a series of images from the Jornada Experimental Range (JER), located in the Chihuahuan Desert of New Mexico, near the town of Las Cruces (fig. 6). This area has experienced dramatic

changes in vegetation cover from semiarid grasslands to arid shrubs. Detailed discussions provided by Buffington and Herbel (1965) and Gibbens et al. (2005) describe the Jornada transition from primarily native perennial grasses (*Bouteloua spp.)* to drought resistant mesquite (*Prosopis glandulosa*) and creosote (*Larrea spp*.). This form of arid land degradation has been attributed to climate change and intensive land use for pastoral purposes.

Figure 6. Location of the Jornada Experimental Range (JER) in south-central New Mexico

This study focuses on the distribution of shrubs in the sand sheet area of the Jornada Basin that comprises the western portion of the JER (fig. 7). The sand sheet exists as a mosaic of patches ranging from mesquite coppice dunes with little to no grass

cover to grasslands with isolated mesquites. There are almost no areas in the JER sand sheet that do not contain some mesquite.
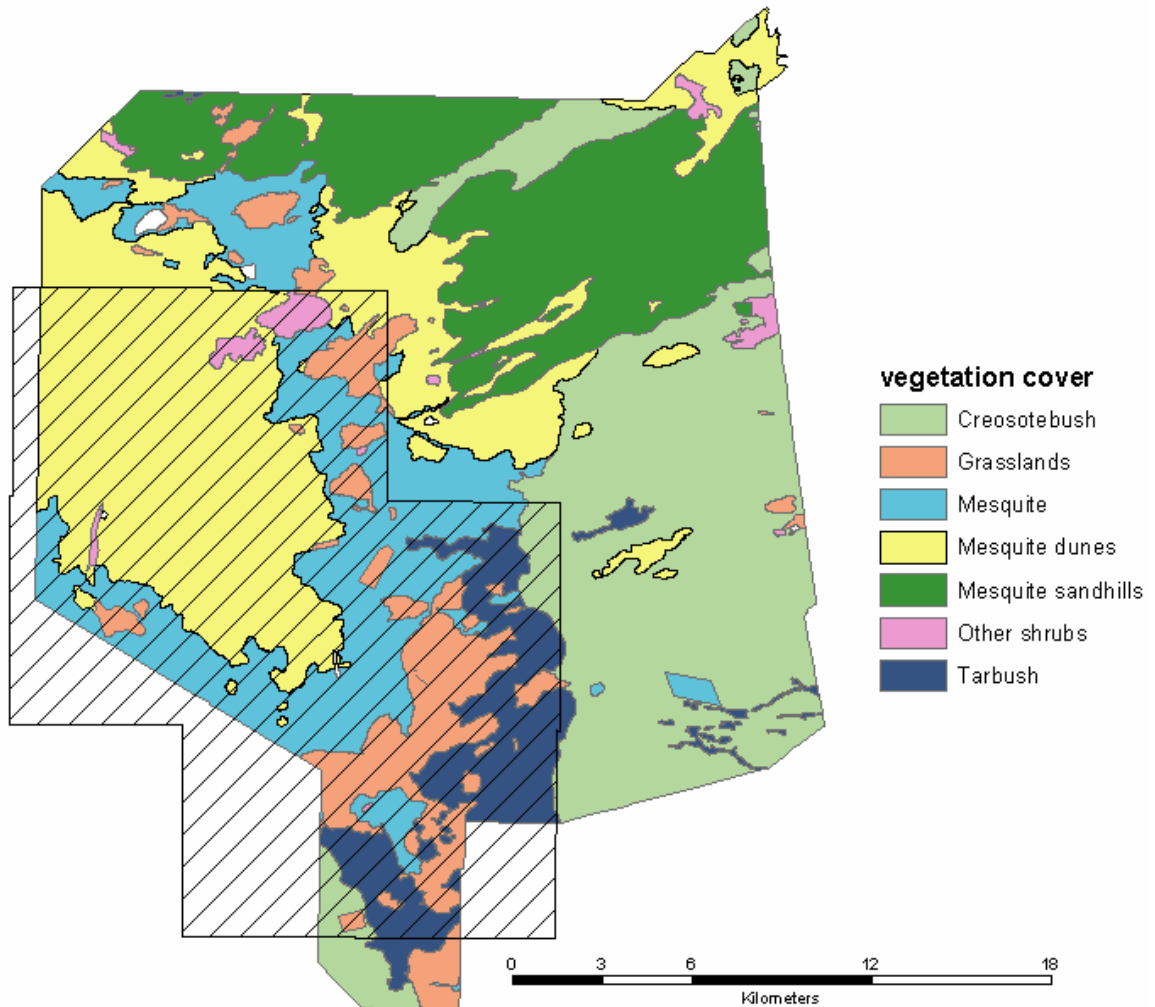
Figure 7. Aerial coverage of digital orthophotos used in this study from October 1996 (striped) and land cover stratification (modified from Gibbens et al., 2005).

2.4. Classification of high-resolution aerial photography

The spatial distribution of vegetation can be ascertained from connectivity calculations of high-resolution aerial photography, which must be first separated into a binary classification of interest. Connectivity can only be calculated for images with a

binary representation of 1 for the class of interest and 0 for all other classes (equation 1). The use of connectivity is independent of the choice of classification scheme. When shrubs are defined as the class of interest, connectivity calculations provide information about the size and shape of shrubs. When the non-shrub classes are defined as the class of interest, connectivity provides information about the size and shape of intershrub patches.

An object-oriented supervised classification was performed on seven digital orthophoto quarter quadrangle (DOQ) natural color aerial photos, originally flown by the USGS in October 1996. One meter ground pixel resolution imagery provides sufficient detail to derive relevant spatial information on mesquite shrubs found in the Jornada sand sheet, as demonstrated by Phinn et al. (1996). Individual mesquite plants larger than 1 m can be identified from the high-resolution imagery and therefore provide an opportunity to examine and extract land cover through both spectral and spatial characteristics through the differentiation of individual shrubs relative to the background of bare soil and grass.

The use of an object-oriented analysis in this study provides many advantages over traditional pixel-based classifications (Geneletti and Gorte, 2003). Object-oriented classification groups adjacent pixels into contiguous multidimentionally homogenous clusters that represent natural land cover patterns and minimize classification errors that result from single pixels with outlier values and areas of complex spectra due to mixed coverage. Thus, this classification procedure can account for the spatial relationship of pixels, not just the spectral values. This method is gaining increasing acceptance as it proliferates throughout the remote sensing community (Dorren et al., 2003) and has been successfully used by Laliberte et al. (2004) at the JER.

For this study, pixels were identified as shrubs or non-shrub cover through a series of segmentation and classifications in the eCognition software (fig. 8). The images were divided into object segments according to size, shape and digital number value from all three visible bands. The segmentation process subdivides the images into groups of pixels based on scale-dependent homogeneity. Single pixels are gradually built-up into larger clusters while accounting for high spectral homogeneity of shrubs relative to soil and the size of shrubs. A maximum object heterogeneity or scale parameter of 6 was used to constrain object sizes and a high emphasis on object compactness and shape to maximize the distinction between shrubs, grasses, and soil. Scale parameter analysis indicated 25% of neighborhoods had a value around 8.62 pixels. All three visible bands had the same spectral weighting for segmentation. Baatz and Schape (2000) provide further description of the segmentation procedure. Supervised classifications were performed on segmented images using a nearest-neighbor approach from the training classes of intensity values for shrub cover, grass cover and soils, and finally grouped according to classes of interest.
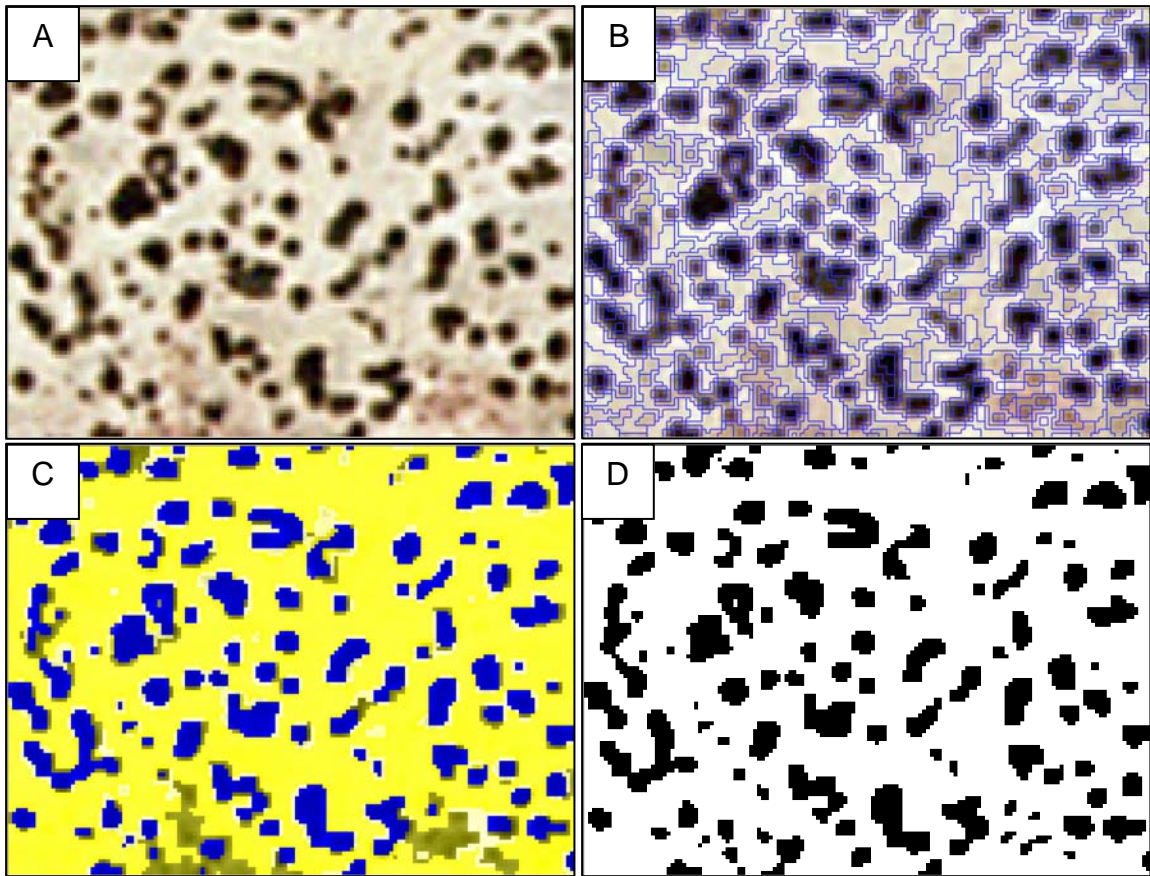
Figure 8. Object-oriented classification process from A) digital orthophoto with darker areas represent shrub patches while the lighter background represents grasses and bare soil, B) image segmentation with irregular shapes representing pixels grouped by shape and similar intensity, C) supervised classification where segments are grouped into regions of shrub cover (dark), grasses and mixed vegetation (intermediate) and bare soil (light) D) extracted binary classification feature of shrub (dark) and no-shrub (light).

While features such as shrubs are easily identified and classified, several limitations are inherent with the use of high spatial-resolution color imagery. Without the availability of high spectral resolution data, it is not possible to accurately distinguish amongst shrub types through a comparison of spectral reflectance. Additionally, centimeter or decimeter-scale vegetation such as grasses cannot be directly detected from meter-scale imagery.

2.5.   Connectivity analysis of classified remote sensing imagery

The classified visible digital images were divided into 200 x 200 pixel subimages in which connectivity was calculated, first with shrubs as the class of interest, then as the non-shrub component as the class of interest. These calculations were performed for lag distances from 0-40 m, at two-degree intervals from 0-360°. Range, elongation, and orientation values for each subimage were then integrated into a new coregistered image with 200 x 200 m pixels. When range, elongation, and orientation are calculated with shrub as the class of interest, these statistics provide information about the size and shape distribution of contiguous areas occupied by shrubs. When these statistics are calculated with the not-shrub as the class of interest, they provide information about the size and shape distribution of intershrub areas that may be comprised of bare soil, grasses, or a mixture of bare soil and grasses.

2.6.   Environmental stratification

The range, geometric elongation, and orientation data were stratified based on a dominant vegetation land cover map, developed from field studies in 1998 (Gibbens et al., 2005). The dominant land cover classification in each subimage was determined and compared with calculated connectivity range, elongation, and orientation. Stratifying orientation and elongation results based on vegetation cover allows for the comparison of shrub distribution within regions of variable shrub infestation.

3. RESULTS

3.1.   Connectivity analysis of simulated images

The connectivity method presented here can determine the direction of anisotropy in simulated images. Figure 9 shows a strong 1:1 relationship between the orientation angle calculated from connectivity and the major-axis of anisotropy used to generate the simulated images (expected angle). The relationship between the range of isotropic variograms used to generate simulated images and the connectivity range is shown in Figure 10. The connectivity range increases with increasing variogram range, but flattens out when variogram range reaches about 10 pixels. The connectivity range is also a function of the fractional cover in simulated images, with lower cover resulting in lower connectivity ranges, when connectivity is calculated on the basis of the cover class. When connectivity is calculated on the basis of the non-cover class, lower cover results in greater connectivity ranges (not shown). These results show that connectivity is able to provide an indication of both the direction of anisotropy and an index of the patch size in simulated images. The index of patch size provided by connectivity (e.g., the connectivity range) is different from that provided by the variogram range used to produce the simulated images. This is due to the fact that connectivity provides a fundamentally different measure of spatial autocorrelation than variograms. Thus, connectivity can be used to augment spatial information from traditional variography and can provide important measures of patch size for categorical data.
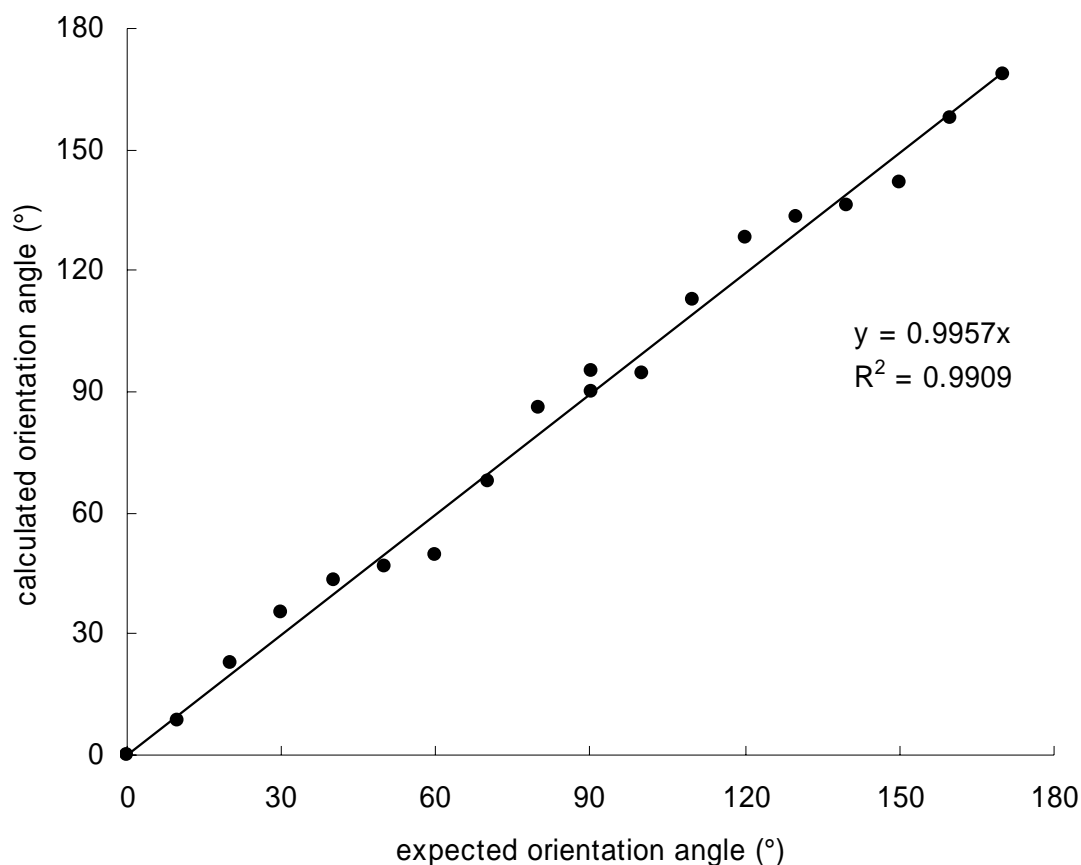
Figure 9. Calculated orientation angle versus expected orientation angle for images created using the simulated annealing algorithm in GSLIB. Expected orientation angle is the angle of the major-axis of the variogram used to create each image. Calculated orientation angle is the angle of orientation determined by the connectivity method presented here. Each point is the mean for three realizations (generated images) at 20% cover.

3.2. Object-oriented classification

The use of 1 m orthophotos imagery provides a suitable resolution to detect the presence of shrubs (Laliberte et al., 2004). Due to the size, grass clumps are difficult to distinguish from the soil background, although further study may overcome this limitation to separate shrubs, grass-covered soils, and bare soils at 1 m resolution. As a result, classification of the orthophotos images with eCognition resulted in maps of the presence or absence of mesquite shrubs, the dominant shrub in the sandsheet are of the

JER. Most of the area was classified as bare soil and grasses, while only 14% of pixel area was classified as shrubs (table 1). Shade dominated pixels may have been misclassified as shrubs in two of the seven images, although unlikely due to visual inspection, spectral differentiation of land cover, the geometric profile of topographically high shrubs, and relatively low leaf area index (LAI) typical of vegetation in October. The maps of mesquite resulted in estimates of fractional cover consistent with other reports (Laliberte et al., 2004; Okin and Gillette, 2001).

Table 1. Major-axis range corresponding to dominant vegetation cover.

land cover class	maximum range (m)		mean range (m)		median range (m)		std. dev.		% cover
	shrub	intershrub	shrub	intershrub	shrub	intershrub	shrub	intershrub	
Grasslands	36.0	327.0	3.5	118.9	2.5	101.3	3.4	83.4	5.2
Mesquite	83.1	325.0	3.1	65.2	2.2	39.7	3.8	69.9	13.4
Mesquite dunes	10.9	227.1	2.5	27.8	2.4	22.8	0.6	20.6	15.0

3.3.   Shrub connectivity range, elongation, and orientation

Connectivity calculations performed on 200 x 200 m subimages using the shrub class as the class of interest provide information on the size and shape of shrub patches. Major-axis, minor-axis, and mean range values for the shrub class are significantly smaller than those for the non-shrub class indicating that mesquite shrubs are generally smaller than the spaces between them (table 1). Median shrub patch size (i.e., median shrub range) does not vary significantly in size with location or the land cover classification from Gibbens, et al. (2005), though the standard deviation of the range is less for mesquite dunes than for either mesquite or grassland areas.
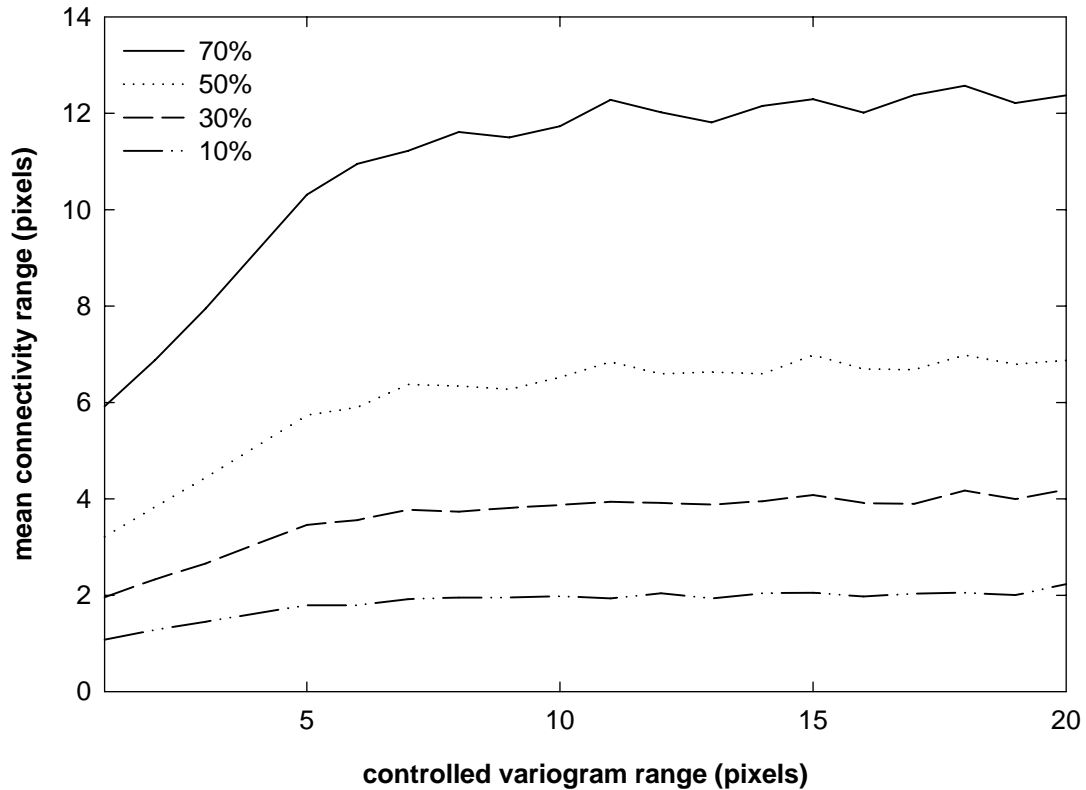
Figure 10. Calculated range distances verses control range sizes for images created using the simulated annealing algorithm in GSLIB. Controlled range is the size of the x and y axes of the variogram used to create each image. Mean connectivity range is the range distance determined by the connectivity method presented here, calculated at 10, 30, 50, and 70% of image cover. Each point is the mean of the major and minor range values for three realizations.

Elongation values are constrained to ≥ 1.0, thus mean and median elongation values are always > 1.0 (table 2). For analysis of elongation values, the ratio of the standard deviation of elongation to the amount that the median value deviates from one provides an index of the organization of the anisotropy akin to the coefficient of variation:

Variability Index (VI) = Standard Deviation of Elongation/(Median of Elongation – 1) (4)

As the VI approaches 1, the anisotropy of shrub or intershrub patches becomes increasingly consistent. Shrub patches tend to be the same size and shape and therefore the VI for the shrub class in all cover types is close to 1.0. Shrub patches in mesquite

areas having the highest value VI = 1.3, which indicates a greater diversity of shrub shapes in these areas.

Table 2. Elongation values for 200 m x 200 m subimages from different land cover classes.

land cover class	mean elongation		median elongation		std. dev.		variability index	
	shrub	intershrub	shrub	intershrub	shrub	intershrub	shrub	intershrub
Grasslands	1.1	2.3	1.1	1.3	0.2	11.5	2.5	46.0
Mesquite	1.1	1.3	1.0	1.1	0.1	2.4	2.7	26.1
Mesquite dunes	1.1	1.1	1.1	1.1	0.1	0.1	1.3	1.2

In subimages dominated by mesquite dunes, the major-axis of anisotropy (e.g., the direction of the greatest range value) is oriented roughly northeast-southwest (fig. 11). For mesquite dune subimages, orientation of shrub patches is clustered between 30° and 59° azimuth and orientation intershrub patches ranges from 0°-59°. In contrast, no clear preferential orientation of shrub patches was detected for those subimages dominated by grass or mixed grass-shrub vegetation.

3.4.   Intershrub connectivity range, elongation, and orientation

Connectivity calculations using the non-shrub classes as the class of interest provide information on the size and shape of intershrub areas. The mean range for intershrub patch size varies significantly with landcover (table 1). Mean and median distances are noticeably larger for areas of grasslands when compared to mesquite and mesquite dunes. The range of intershrub patch size (e.g., the mean distance between shrubs) decreases from 119 m in mixed vegetation to 65 m in mesquite, and 28 m in mesquite coppice dunes. Median range decreases from 101 m in grass-dominated areas to 40 m in mesquite-dominated areas to 23 m in areas dominated by mesquite dunes. The smaller intershrub distances in mesquite dunes indicate a higher density of shrubs in regions of mesquite and mesquite dunes with respect to areas of grasses. Where shrub
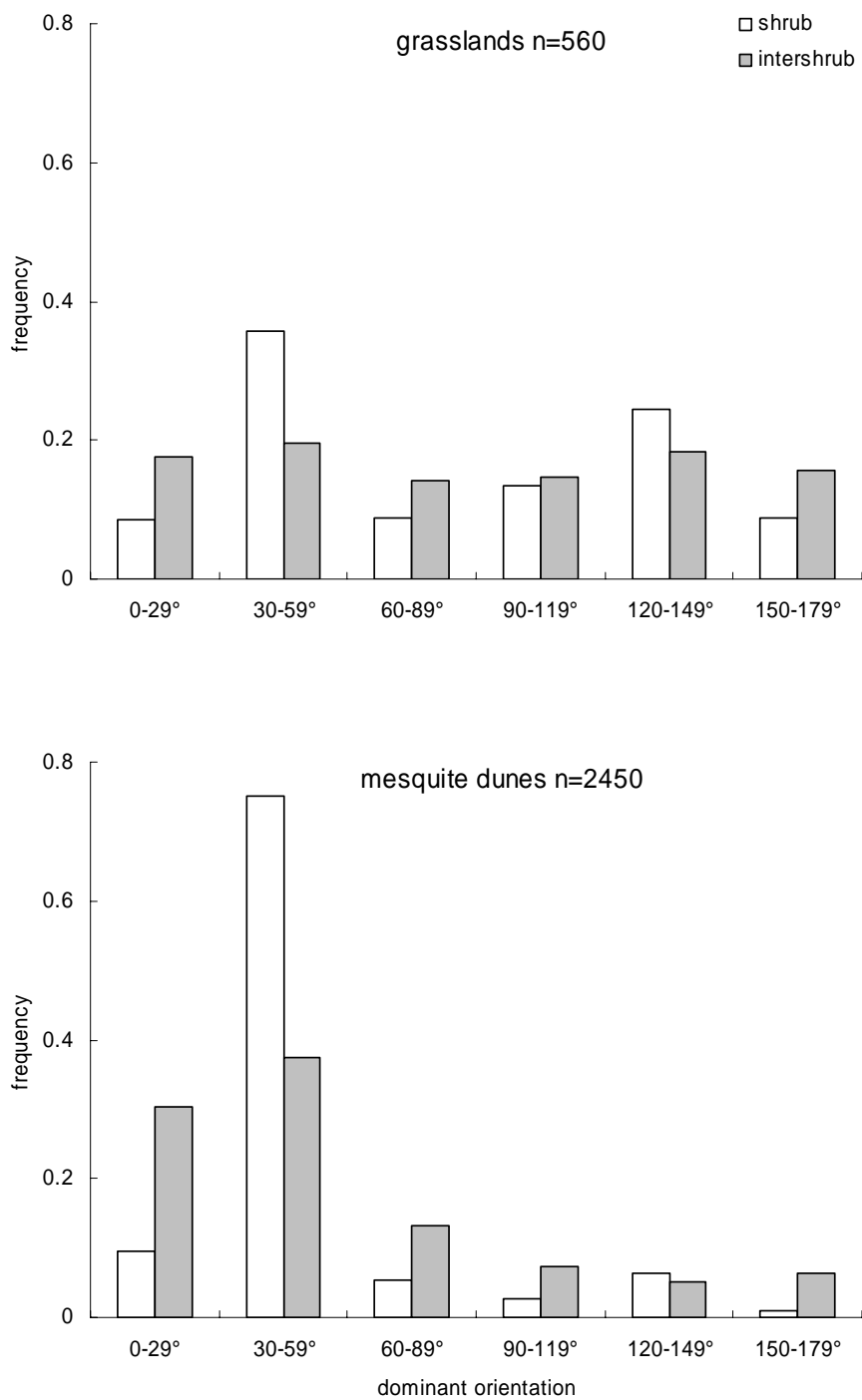
Figure 11. Histogram of orientation for shrub and intershrub patches for grasslands and mesquite which indicate no preferential orientation, and mesquite dunes showing strong preferential orientation.

size is nearly constant, intershrub distances are inversely related to plant density reflecting an increasing continuum in shrub number density from grasslands to mesquite dunes.

VI (equation 4) calculated from elongation values for intershrub patches in areas dominated by grassland and mesquite all deviate significantly from 1.0 indicating a large diversity in intershrub patch shape in these areas. In mesquite dunelands, VI = 1.3 indicates a consistent intershrub patch shape in these areas, with a slight elongation of 1.1. Values of VI > 1.3 for intershrub areas in non-dunelands is consistent with irregular mesquite invasion in these areas and increasingly regular, but anisotropic, mesquite establishment, as mesquite density increases until the VI = 1.2 in mesquite dunelands.

Orientations of intershrub patches clearly shows a variation between landcover types, generally similar to the orientation differentiation of the shrub class of interests (fig. 11). A lack of clear preferential orientation is present in grassland and mesquite regions. The strong orientation found for shrubs in a general SW-NE orientation in mesquite dunes cover is also present for intershrub areas in this landcover type.

4. DISCUSSION

Connectivity calculations performed on high resolution digital images provides information on the size and shape of both shrubs and intershrub patches. Stratified by dominant landcover types, variations in shrub and non-shrub distribution reflect the progressive nature of the transition from grassland to shrubland, evident throughout the JER (Gibbens et al., 2005; Laliberte et al., 2004).

Analysis of 1-m orthophotos also provides a direct measurement of the anisotropy of mesquite distribution in the sandsheet portion of the JER. Dominant orientations suggest that the presence of isotropic and anisotropic spatial distribution can be detected using the method presented here. The strength of this anisotropy requires explanation and clearly disputes the widely-used assumption of homogeneous (Gillette and Stockton, 1989; Musick and Gillette, 1990b) or random (Marticorena and Bergametti, 1995) distributions of land cover in models.

The influences of spatial patterns of vegetation have significant implications for aeolian emission and transport modeling of arid landscape degradation. Shrubs and intershrub patches in areas of mesquite coppice dunes show a strong northeast-southwest orientation, and agreeing with earlier studies by Okin and Gillette (2001) and Gillette and Pitchford (2004) that suggested the existence of areas of bare soil with strong windward orientation within regions of mesquite cover called "streets".

The isotropic orientations found in grasslands indicate a lack of dominant orientation, resulting in a homogeneous or random distribution of mesquite cover. The lack of a dominant orientation in regions of mesquite and amongst grassland vegetation indicates that streets have not developed in these areas. The strong preferential orientation in mesquite dunelands in the Jornada Basin indicates the widespread presence of streets in these areas.

The connectivity results reflect the physical characteristics associated with the respective vegetation cover and must therefore be incorporated within future models of vegetation dynamics and aeolian geomorphology, in addition to providing potential applications beyond aeolian geomorphology. Successful models of landscape dynamics

in areas that exhibit strong anisotropy must be able to reproduce these patterns of anisotropy.

Mesquite shrublands dominate, control, and possibly destroy their surrounding environment (Reyes-Reyes et al., 2002; Schlesinger et al., 1990). Connectivity statistics document a marked spatial progression of land cover development. The propagation and development of mesquite shrubs is part of a clear transitional process, influenced by both biotic and abiotic forces, evident in the JER.

Large intershrub distances found in grasslands indicate low shrub density and ideal locations for the establishment of shrubs. Ecological field tests suggest bare soil and to a lesser extent grasslands are regions that allow for root development, soil moisture and nutrient uptake of shrubs with minimal competition from woody vegetation (Schlesinger and Pilmanis, 1998). This initial biotic control is augmented by abiotic factors such as wind erosion, with increased drag and subsequent trapping of water and airborne particles under individual shrubs. Once established, shrubs may cohabitate with grasses and mixed vegetation, but have been observed to be more resilient to environmental and ecological changes, and may therefore allow shrubs to endure even as grasslands are destroyed (Schlesinger et al., 1990; Whitford, 1992).

Relatively constant shrub size across landcover types indicate that mesquite shrubs reach a characteristic size (the range) relatively quickly that generally does not vary over time, even as shrub infestation progresses. Furthermore, since grasslands, mesquite-dominated areas, and mesquite dunelands belong to a continuum of shrub infestation, the results presented here clearly indicate that this process occurs by continual infilling. The process of infilling is distinct from two other conceptions of shrub

encroachment: 1) shrub encroachment occurs as an advancing front, and 2) shrub recruitment occurs everywhere in a grassland but the individuals do not increase in size until some threshold is reached when shrubs become dominant and individuals all grow to large size simultaneously. In contrast, infilling is seen as a process where recruitment happens continuously in the landscape and mesquite grow to a large size relatively quickly after successful recruitment.

The progressive development of anisotropic shrub distributions along the grass-mesquite-mesquite duneland continuum strongly indicates that certain sites exhibit higher probability of mesquite establishment than other sites. The correspondence between the major axis of anisotropy in mesquite dunelands and the direction of the prevailing wind at Jornada implicates aeolian transport as a strong control on shrub establishment. Several mechanisms associated with aeolian processes may contribute to the progressive development of anisotropy:

1) Seed dispersal: Although mesquite seeds or seedpods are not particularly prone to dispersal by wind, strong wind events do transport seeds either by creep or saltation. Seeds transported in this way would tend to be removed from high-energy locations in between shrubs and deposited in low-energy locations under or in the lee of existing vegetation. The distribution of high- and low-energy environments with respect to aeolian transport will be highly oriented in the direction of the prevailing wind direction, resulting in the anisotropic dispersal of seeds.

2) Lee-side deposition: The deposition of organic material and fine-grained mineral aggregates in the lee of established mesquite may create suitable

microenvironments for the establishment of mesquite by creating areas of high nutrient content and high water holding capacity in these areas.

3) Abrasion and scouring in intershrub areas: The high-energy wind environments exhibited in unvegetated areas in between shrubs create streets of high sediment transport (Gillette & Pitchford, 2004). Abrasion of vegetation may increase seedling mortality in these high-energy locations resulting reduced mesquite survival.

The mesquite dunelands in the Jornada sandsheet most likely represent the final stage of the infilling process, due to the highest degree of anisotropy and the highest density of mesquite shrubs. It is unknown at this time whether biotic processes such as competition for water or abiotic processes such as aeolian transport terminate shrub infilling. However, the study of sediment transport in intershrub streets in mesquite dunelands by Gillette and Pitchford (2004) suggests that increased aeolian transport in intershrub areas is a strong candidate.

As the region shifts from homogenous grasslands, shrub encroachment likely disrupts the spatial distribution of nutrients and soil moisture into a heterogeneous clustering in which the distribution of shrubs is influenced by biotic and abiotic processes with varying degrees of anisotropic behavior. This clustering, anchored by the establishment of shrubs creates islands of fertility. Intershrub regions become exceedingly vulnerable to dust emissions and the erosive removal of nutrients and soil moisture.

The loss of exposed topsoil by aeolian processes in intershrub regions inhibits grasslands while encouraging the development of islands of fertility and indicates a major shift from biotic to abiotic influences. Due to the presumed domination of abiotic transport processes within the JER, a strong dichotomy of elongation and orientation would be expected, and is found for shrub cover amongst differing areas of dominant vegetation cover. The detected anisotropy of shrub and intershrub areas that correlates with the prevailing wind direction further indicate the importance of abiotic transport. The dominant preferential orientation detected in areas of mesquite dunes roughly parallels the southwesterly prevailing winds. The absence of a strong preferential orientation in grasslands and moderate orientation in mesquite dominated areas reflects the transitional model for desertification presented by Okin and Gillette (2001) and Schlesinger, et al. (1990).

In the progression from homogeneous landscape of grasses to a heterogeneous landscape of shrublands, aeolian processes become increasingly relevant, forcing the moderate orientation of shrubs in the mesquite regions to the highly-oriented shrubs in the well-established mesquite dunes region. The increased propagation of shrubs reduces the connectivity in grasslands. A continuous infilling of shrubs in grasses and mixed vegetation is evident. While the shrubs do not seem to get detectably larger, they force the transition from a biologically controlled region to an aeolian controlled region in which the environment impacts the vegetation and the environment. Ultimately, in developed mesquite coppice dunes, shrub cover itself becomes the dominant control on surface geomorphology.

5. CONCLUSION

The statistical method presented here for calculating landscape connectivity provides a valuable method to quantify spatial connectedness from raster datasets. With appropriate datasets and classification, potential applications extend beyond vegetation dynamics to other areas of the biological and earth sciences, including preserve planning, habitat fragmentation, pore spacing in surface hydrology, microbial community dynamics and other areas where the understanding of the size and arrangement of patches is important.

The primary use of connectivity in this study has been to quantify the spatial distribution of shrubs to provide further insights into process of shrub encroachment in the JER in south-central New Mexico. While complex interaction of multiple biotic and abiotic forces are responsible for shaping the vegetation communities in the JER, the importance of abiotic processes such as aeolian transport become clear in the anisotropy of shrubs and intershrub patches. The spatial distribution and preferential orientation of shrubs in the Jornada Basin that has been demonstrated here provides evidence for infilling as an important component of shrub infestation. Our results also provide a prediction that areas dominated by mesquite in the sandsheet will develop into mesquite coppice dunelands. We anticipate that this will correspond to an increase in aeolian transport and dust emission in these environments.

Woody encroachment is not exclusive to New Mexico and has been observed in areas such as Texas (Ansley et al., 2001), southern Africa (Roques et al., 2001), Argentina (Cabral et al., 2003), and Austraila (Fensham et al., 2005). Integration of connectivity into models of geomorphology and vegetation dynamics in these areas will

provide further insight into land degradation processes in arid and semiarid environment, and to achieve comprehensive desertification models.

CHAPTER 3

Influence of vegetation spacing on wind erosion

(Portions of this chapter are to be submitted in Journal of Geophysical Research.)

Abstract

Wind erosion, the primary geomorphic forcing mechanism in arid environments, can be greatly reduced by the presence of vegetation. The entrainment of small mineral dust aerosols into the atmosphere results from the saltation of small particles that impact a surface during sandblasting. Roughness elements such as vegetation or large rocks decrease the availability of saltation particles, shelter leeward surfaces, and extract moving particles. Changes in shear stress over roughness elements relative to a bare surface have been used as a method to represent and model the effects of vegetation on dust flux. Most models are unable to account for the inhomogeneous nature of vegetation distribution, and overestimate the prediction of dust emissions. A new method of dust flux is presented to incorporate possible scenarios of spatial distributions of vegetation from probability gap spacing. A Poisson distribution of flux, agreed with field data and with observations in literature. Shear stress inhomogeneity (m) was found to be reduced with low and high lateral cover ($0.1 < \lambda < 0.3$) and maximized at $\lambda = .15$, 0.3 for Poisson and uniform distributions. Homogeneous wind regimes were modeled from surfaces of low cover with isolated individual wakes, and of high cover with overlapping wakes creating skiming flow. Intermediate cover was most inhomogeneous with high distortions of wind flow from interference wakes.

1. INTRODUCTION

Wind erosion is a dominant mechanism of sediment transport in arid environments. Understanding the land surface factors that control wind erosion is vital in understanding both land degradation processes in deserts and the global loading of mineral aerosols. Aeolian transport contributes to land degradation through the abrasion and burial of vegetation by saltating particles as well as the removal and redistribution of nutrient-rich particles in fine sediment (Li et al., submitted; Okin et al., 2001a). Mineral aerosols, also known as desert dust, produced by sand-blasting of fine particles from the surface during saltation, impact the planetary albedo and radiation balance (Bellouin et al., 2005; Haywood and Boucher, 2000; Kaufman et al., 2002), may also suppress precipitation (Rosenfeld et al., 2001), and can transport soil nutrients to far downwind ecosystems (Okin et al., 2004).

Vegetation or other nonerodible elements have a direct impact on the erodibility of a surface and emission of dust into the atmosphere (Wolfe and Nickling, 1993). Vegetation reduces the availability of erodible particles. Wake formations in the lee of plants create areas that are sheltered from erosion. Vegetation also extracts momentum from the wind. Finally, transported particles can become trapped by vegetation and removed from the airflow (Raupach et al., 2001). Refining the models of dust emissions can improve predictions of how global land cover change will impact mineral aerosol loadings and provide information on how to mitigate land degradation in arid and semiarid lands.

Aeolian transport is initiated when the wind shear velocity (u_*) exceeds the threshold shear velocity (u_{*t}). The threshold of particle transport in the absence of

vegetation, the soil erodibility can be impacted by several factors such as soil texture (Alfaro and Gomes, 2001; Leys and McTainsh, 1996), mineralogy (Gillette, 1997) and moisture (Ravi and D'Odorico, 2005). Above the threshold shear velocity three aeolian transport processes observed by (Bagnold, 1941) govern the fundamental erosion and movement of mineral dust aerosols: suspension, saltation, and creep.

Saltation is initiated when the lift provided by wind exceeds the forces of gravity and cohesion holding the particle to the surface (Cornelis and Gabriels, 2003). The most efficient saltators, those with the lowest threshold shear velocity, have a diameter of about 70 μm, but most saltation sized particles are 50 to 500 μm (Raupach and Lu, 2004). Saltation can be augmented when moving particles collide with particles at the surface, transferring momentum and kinetic energy. Particles that are ejected from the surface are entrained by saltation bombardment. Larger particles are said to move by "creep" when they are nudged by impacting saltators.

The natural emission of suspended dust material occurs primarily as a product of saltation bombardment and not from aerodynamic lift. The vertical flux of dust particles is directly proportional to horizontal flux (q), as the energy imparted by saltation bombardment exceeds gravity and cohesive interparticle bonds through collision (Gillette et al., 1996; Raupach et al., 1993; Shao et al., 1993).

Shear stress partitioning has been the primary process in which extraction of momentum from the wind by vegetation has been modeled. In this approach, the total shear stress $\tau = F/A$ of the wind is apportioned into the force acting upon the vegetation (F_v) and that acting on the bare surface (F_s), in a given area A. The ratio of the shear stress acting on the surface to the total shear stress (τ_s/τ) is known as the shear stress

ratio, *R*. Raupach (1992) and Raupach et al., (1993) have used the shear stress partitioning approach to evaluate the ratio of threshold friction velocity for a vegetated surface, u_{*tv}, relative to that on bare surfaces u_{*ts}. In the model, the partitioning of shear stress is related to the roughness density and momentum extraction is controlled by the drag on the surface created by the streamwise lateral area of roughness surface elements per unit area (lateral cover, often denoted by λ). Lateral cover is usually defined as:

$$\lambda = \frac{nbh}{S} \tag{1}$$

with the mean physical dimensions of roughness elements width *b*, height *h*, number *n*, per surface unit area *S*. Okin (2005) has provided an equivalent definition: $\lambda = NA_p$, where *N* is the plant number density and A_p is the profile area of plants (*bh*).

Although the research of Raupach et al. (1993) did not directly address the distribution of shear stress at the soil surface, a correction variable, the *m* parameter, was presented to address this concern. Specifically, *m* is defined as the threshold shear stress for a particular surface, $\tau_s^{"}$, equal to the threshold shear stress for a less dense (lower λ, m $\leq$1) surface,:

$$\tau_s^{"}(\lambda) = \tau_s^{'}(m\lambda) \tag{2}$$

The threshold friction velocity ratio for erodible and nonerodible surfaces is expressed as:

$$R_t = \left(\frac{\tau_s^{"}}{\tau}\right)^{1/2} = \frac{u_{*ts}}{u_{*tv}} = (1 - m\sigma\lambda)^{-1/2}(1 + m\beta\lambda)^{-1/2} \tag{3}$$

where σ is the average basal area to profile area ratio for roughness elements, and $\beta = C_R/C_S$ is the ratio of the drag coefficient of a single roughness element to the drag coefficient of the erodible surface in the absence of vegetation.

Interpreted as a surface inhomogeneity parameter, Raupach et al. (1993) originally estimated *m* to be close to 1.0. Experimental measurements of the *m* parameter

by Crawley and Nickling (2003) suggest that m=0.5 to 0.6 when λ is close to 0 and m = 0.2 to 0.3 as λ approaches 0.05. The empirical fit of m=0.16 from Wyatt and Nickling (1997) is much lower than those of Crawley and Nickling (2003), which may result from the enhanced effect from wake development downwind of porous vegetation. Approaching an interpretation of m from the averaged surface shear stress ratio suggests the original concept of m may be inherently problematic for nonuniform roughness elements, which cannot be constant over a surface (King et al., 2005).

Several assumptions inherent in the Raupach et al. (1993) shear stress partitioning model present difficulties in accurate characterizations of stress behavior in vegetated surfaces. For instance, the m parameter accounts for inhomogeneities in the shear stress on a vegetated surface, and is intended as a landscape-scale correction factor for these inhomogeneities. However, shear stress changes as a function of leeward distance from a shrub (Bradley and Mulhearn, 1983) (fig. 1). A constant m value may not be appropriate for estimating the inhomogeneous effect of vegetation on the ratio of shear stress on total bare surfaces. The m parameter is ultimately a correction value based neither on physical surface characteristics or shear stress theory (Cleugh, 1998).
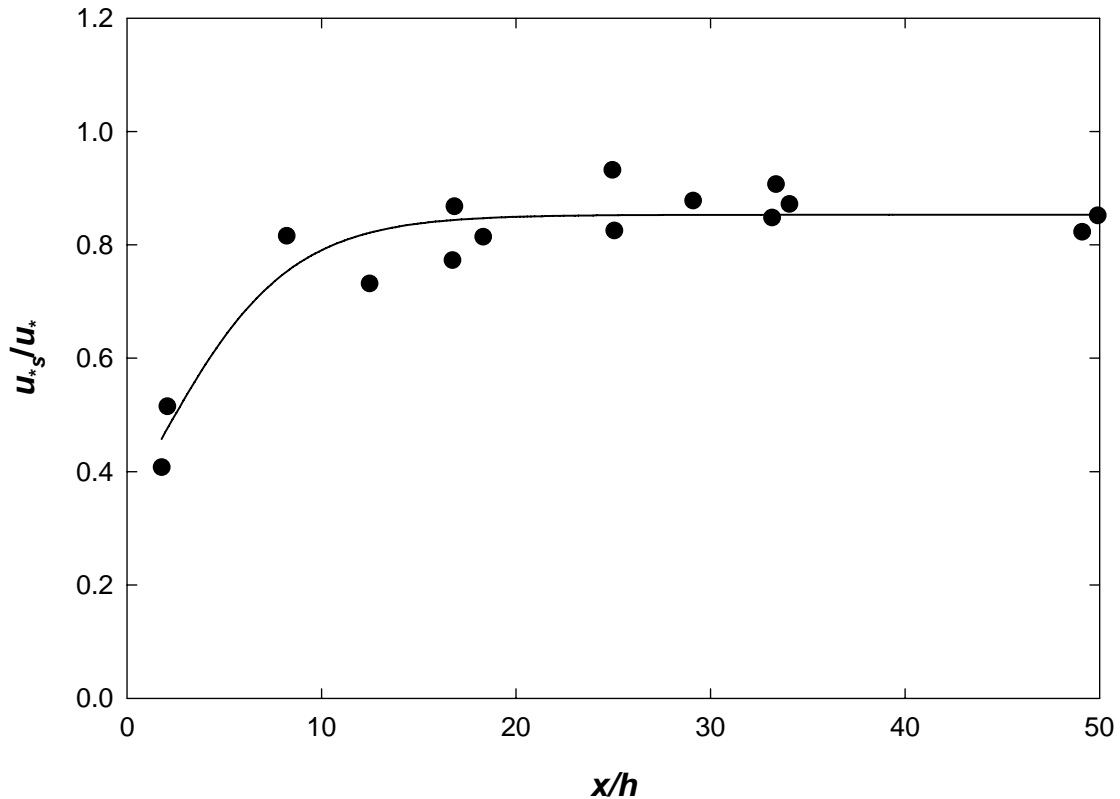
Figure 1. The ratio of surface shear velocity to shear velocity u_{*s}/u_* for distance downwind of fences expressed in terms of fence heights, *x/h*, under conditions of neutral thermal stability (from Bradley and Mulhearn, 1983).

Furthermore, in the shear stress partitioning model of Raupach (1992) and Raupach et al.(1993), lateral cover, λ, describes the density of roughness, but not the distribution of surface roughness elements. Momentum extraction (Raupach et al., 1993) and the sheltering effect (Wolfe and Nickling, 1993) are likely to be highly variable in space, relative to the exact location of vegetation. The size of the sheltered still area in the lee of vegetation and the extended wake area beyond that are controlled by the height and width of vegetation (Cleugh, 1998; McNaughton, 1988; Raupach, 1992), and depending on the lateral and vertical vegetation distribution, the fraction of the ground surface that is influenced by the wake. Lateral cover, being a simple "landscape scale" parameter, cannot differentiate between several small objects or a few large objects, nor can lateral

cover indicate how vegetation is distributed on the landscape (i.e., randomly, regularly, or clustered) (figure 2).
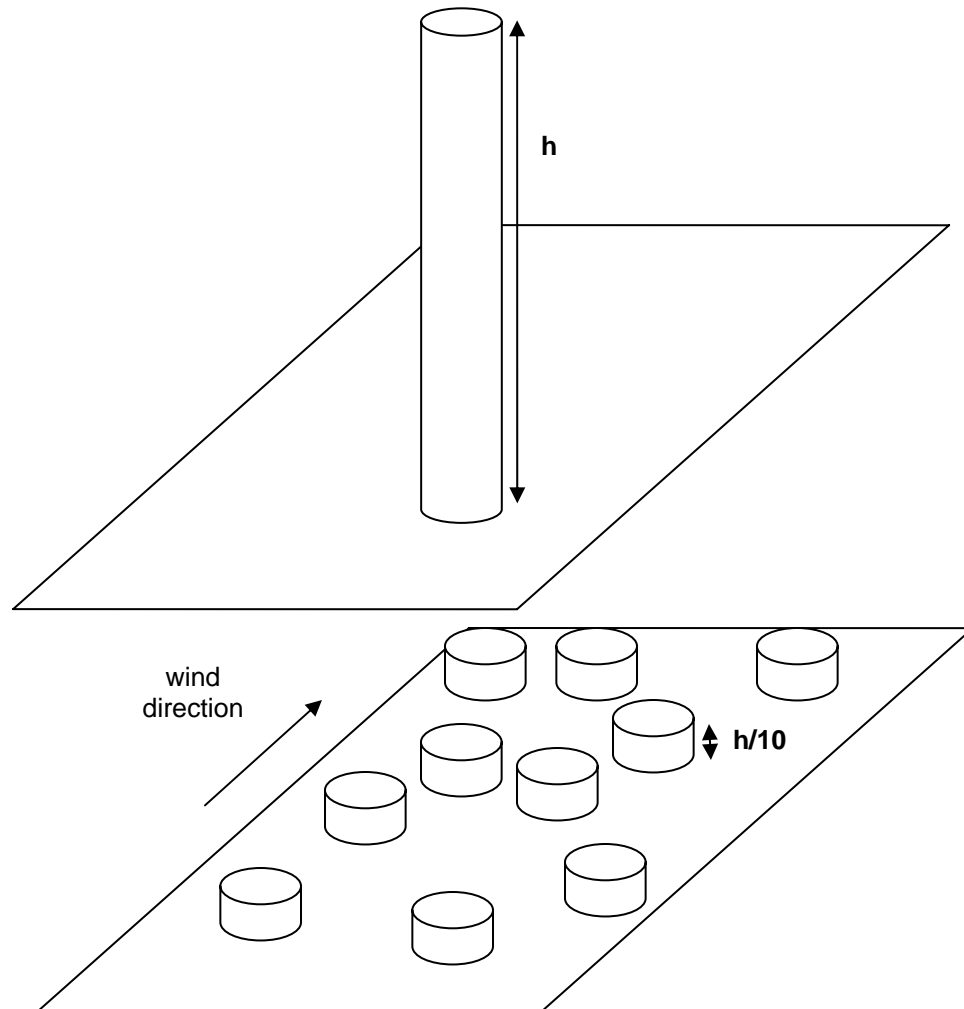
Figure 2. The lateral profile of several small roughness elements (bottom) can be the same as the profile area for few large elements (top), but these conditions will provide difference degrees of protection from erosion.

Despite the fact that lateral cover does not specify how vegetation is arranged on the surface, the use of lateral cover does imply certain factors about how vegetation is distributed. First, lateral cover implies that vegetation is arranged in well-defined clumps on the surface with bare areas between these clumps. Second, lateral cover and the σ ratio in the Raupach et al. (1993) shear stress partitioning model imply that the vegetation has some easily-defined geometry, specifically with a rectangular profile and, often, a

round basal area (i.e. cylindrical in form). Third, vegetation is comprised of plants that are all roughly the same size and geometry, without significant grass cover in the wake of the mesquite bushes. Fourth, vegetation clumps are randomly arranged.

2. METHODS

2.1. Model description

In this study, we investigate how the spacing of vegetation might be included in models of aeolian flux to improve predictions of flux from natural surfaces. The new model, denoted "$Q=f(x)$", that we develop uses a probabilistic approach to calculate landscape-scale horizontal flux, Q, based on fluxes from unvegetated gaps of specific sizes, $q(x)$, and the probability distribution for unvegetated gaps, p(x):

$$Q = \int_0^\infty q(x)p(x)dx \tag{4}$$

This approach essentially builds on the suggestion by Raupach and Lu (2004) that the landscape should be divided into homogenous units and be given probabilistic weights proportional to the relative area of these units.

2.2. Probability of gap size

For modeling purposes, any probability distribution of gap sizes may be used, however, a distribution that accurately represents the actual gap size distribution is preferred. Here, we use three different gap-size probability distributions:

1) Gaps are all equal size, L: $P(x) = \begin{cases} 0 & x = L \\ 1 & x \neq L \end{cases}$ (5)

2) Gap size is defined by a Poisson distribution with the most likely gap size equal to L and an average gap size equal to $\overline{L} = L$:

$$P(x) = \frac{e^{-L} L^x}{x!} \tag{6}$$

3) Gap size is defined by the following curve with the most likely gap size equal to L:

$$P(x) = \frac{x e^{-L/x}}{\int\limits_0^\infty x e^{-L/x} dx} \tag{7}$$

This probability distribution is derived from an exponential decrease in gap "connectivity" observed by (McGlynn and Okin, 2006). For this distribution and all other arbitrary gap size probability distributions, the average gap size, $\overline{L}$, is equal to:

$$\overline{L} = \int\limits_0^\infty x P(x) dx \tag{8}$$

A relationship exists between the average gap size for any probability distribution, $\overline{L}$, and lateral cover, λ. Consider a line transect across vegetation arranged in columnar clumps, all of roughly the same size. The average length of a gap and the adjacent (upwind) plant, $\overline{D}$, will be given by:

$$\overline{D} = \overline{L} + \overline{W} \tag{9}$$

where $\overline{W}$ is the average streamwise width of a plant and, $\overline{L}$ is the average streamwise width of a gap. For a circle of diameter $d = 1$ m, $\overline{W} = 0.574 d$, as the probability of a line intersecting any point within the circle basal area.

Based on these definitions, the number density of plants in the streamwise direction is given simply by $N = (\overline{D})^{-1}$. The fractional cover of plants, C, is the fraction of the length of a line parallel to the direction of the wind that is covered by plants, and is given by:

$$C = \frac{\overline{W}}{\overline{L} + \overline{W}} = \overline{W}N \tag{10}$$

Okin (2005) and Lancaster and Baas (1998) have shown that relationship exists between C, and lateral cover λ:

$$\lambda = \frac{A_P}{A_B}C \tag{11}$$

where A_P is the average profile area of plants, and A_B is the average basal area of plants. For cylindrical plants, the basal area is equal $\pi d^2/4$ and the profile area, is given by dh. Thus, the ratio for these plants of A_P/A_B is given by $(4/\pi)(h/d)$. Combining equation 11 with the definition of C yields:

$$\lambda = \frac{A_P \overline{W}}{A_B\left(\overline{L} + \overline{W}\right)} \tag{12}$$

Rearranging to solve for $\overline{L}$ yields a relationship between $\overline{L}$ and λ:

$$\overline{L} = \overline{W}\left(\frac{A_P}{A_B \lambda} - 1\right) \tag{13}$$

The relationship between $\overline{L}$ and λ is plotted in figure 3.
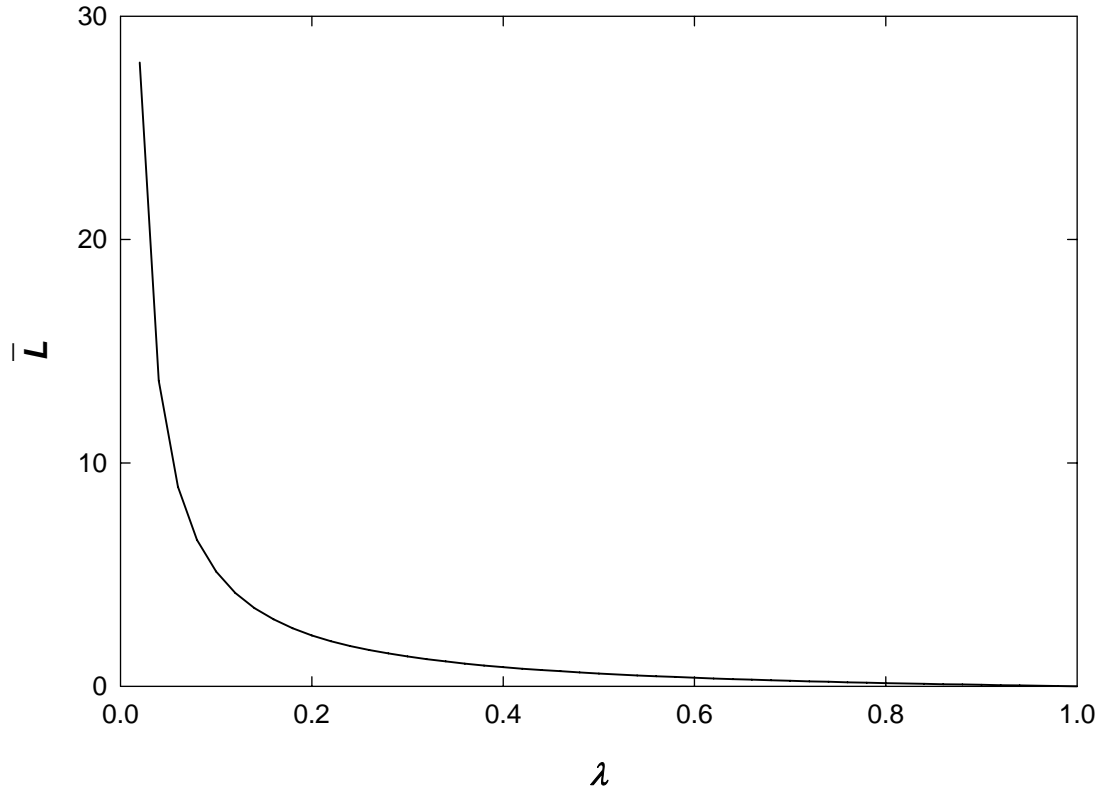
Figure 3. The average streamwise width ($\overline{L}$) versus lateral cover (λ), assuming diameter $d=1, \overline{W} = 0.574d$, and plant area ratio $A_P/A_B=1$.

2.3.   Horizontal flux

Based on considerations of conservation of momentum under steady-state saltation (Shao et al., 1993), horizontal dust flux is modeled as:

$$q = Ku_* \left(u_*^2 - u_{*tv}^2 \right) \tag{13}$$

when u_* exceeds the threshold shear velocity, u_{*tv}, and where $K = A\rho/g$, A is a dimensionless constant with value approximately equal to 1, ρ is the density of air, and g is the acceleration due to gravity. In our model, we modify equation (13) slightly, so that q and u_{*tv} are functions of gap size, x:

$$q(x) = Ku_* \left(u_*^2 - (u_{*tv}(x))^2 \right) \tag{14}$$

Rearranging equation 3 and expressing m as a function of gap size returns a distance dependent threshold friction velocity for vegetated surfaces.

$$u_{*_{tv}}(x) = u_{*_{ts}}\sqrt{(1-m(x)\sigma\lambda)(1+m(x)\beta\lambda)} \qquad (15)$$

Shear stress changes as a function of leeward distance from a shrub resulting from nonerodible sheltered areas, and the creation of downwind wakes (fig. 4). With changes in shear stress with distance, m cannot be assumed to be constant, but is instead a function of gap size: $m(x) = f(x)$. Fences have long been erected as barriers to stabilize soil and reduce wind erosion. As solid and semi-permeable structures, fences can represent many of the roughness-sheltering behaviors observed in vegetation. Like vegetation, fences create downstream wakes, with porous fences more effective in sheltering erodible surfaces than solid buffers (Bradley and Mulhearn, 1983). The sheltered areas experience reduced turbulence, in addition to decreased water vapor and CO_2 flux, and reduced sandblasting (Cleugh, 1998). The sheltering influence of vegetation decreases with distance, with a sheltered area in the immediate downwind shadow of the fence and an extended wake area extended beyond the sheltered area.
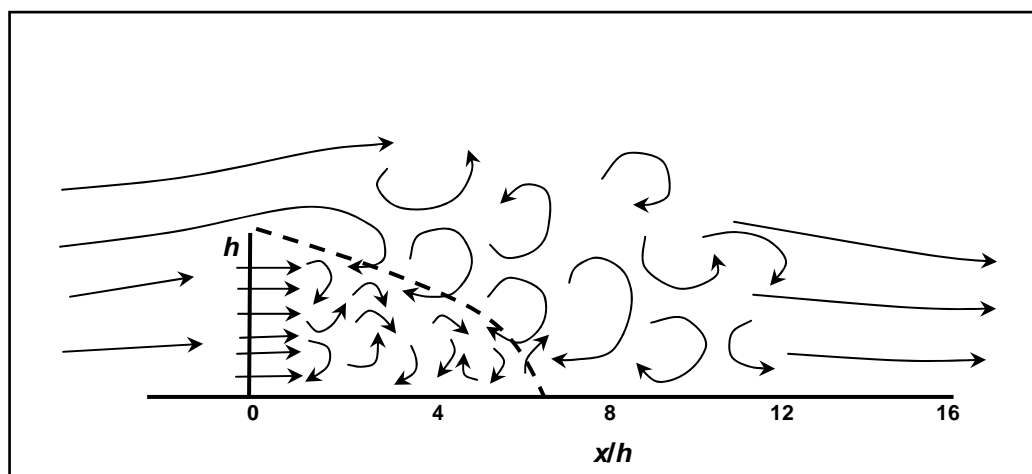
Figure 4. Surface barriers such as fences or vegetation create sheltered areas and the development of downwind wakes (from McNaughton, 1988).

In their review of the impact of porous fences on airflow, Bradley and Mulhearn (1983) show that significant wind shear can exist in the lee of fences (fig. 4). Roughness elements such as vegetation or fences, create leeward recirculating eddies with surface and separation streamlines reattaching at $x/h = 6$ to 7, and reports of surface shear stress differences as far as $x/h=50$. This implies that the m parameter is also a function of gap size. In order to estimate how m might vary as a function of x, we inverted the results from Bradley and Mulhearn (1983) in figure 1 and fit a three parameter sigmoid curve through the inverted data:

$$m(x) = \frac{a_2}{1+e^{a_0+a_1x}} + a_3 \tag{16}$$

where a_0, a_1, a_2, a_3 are fitting coefficients with values: -0.7, 0.7, 1.1, and 0, respectively.

2.4.   Estimation of an effective landscape-scale m parameter

In our new $Q=f(x)$ model, the m parameter is assumed to be a function of gap size. In order to compare our model with that of Raupach et al.(1993), we have defined an effective landscape-scape m paramter, m_{eff}, that would yield a value of $q=Q$ for the same values of u_*, u_{*ts}, λ, σ, and β. m_{eff} is derived simply by plugging the Raupach et al.(1993) equation for u_{*tv} (eq. 15) into the Shao et al.(1993) horizontal flux equation (eq. 13), and solving for m. When q equals Q, m_{eff} is equal to m and can be expressed as:

$$
\begin{aligned}
m_{eff} = &\frac{\left(-\sigma\lambda Ku_{*ts}^{2}u_*\right)+\left(\beta K\lambda u_{*ts}^{2}u_*\right)}{2\beta\sigma K\lambda^{2}u_{*ts}^{2}u_*} \\
&\pm\left[\left(\left(\sigma\lambda Ku_{*ts}^{2}u_*\right)-\left(\beta K\lambda u_{*ts}^{2}u_*\right)\right)^{2}-\left(\left(4\beta CK\lambda u_{*ts}^{2}u_*\right)\left(-Q-Ku_{*ts}^{2}u_*+Ku_*^{3}\right)\right)\right]
\end{aligned}
\tag{17}
$$

2.5.   Field observations

Flux observations from Big Spring Number Eight (BSNES) collectors were recorded in the Chihuahuan Desert of southern New Mexico at Jornada Experimental Range (JER) for a period of approximately 3 months during the spring and summer of 2005. Simultaneous measurements of vegetation allowed estimation of the mean gap size, $\overline{L}$ (fig.5). Similar results have also been reported from Lancaster and Baas (1998) from a low vegetation sandsheet in dried Owens Lake, California (fig. 6). These results will be used here, along with field results from Jornada as a preliminary check of the model presented here.
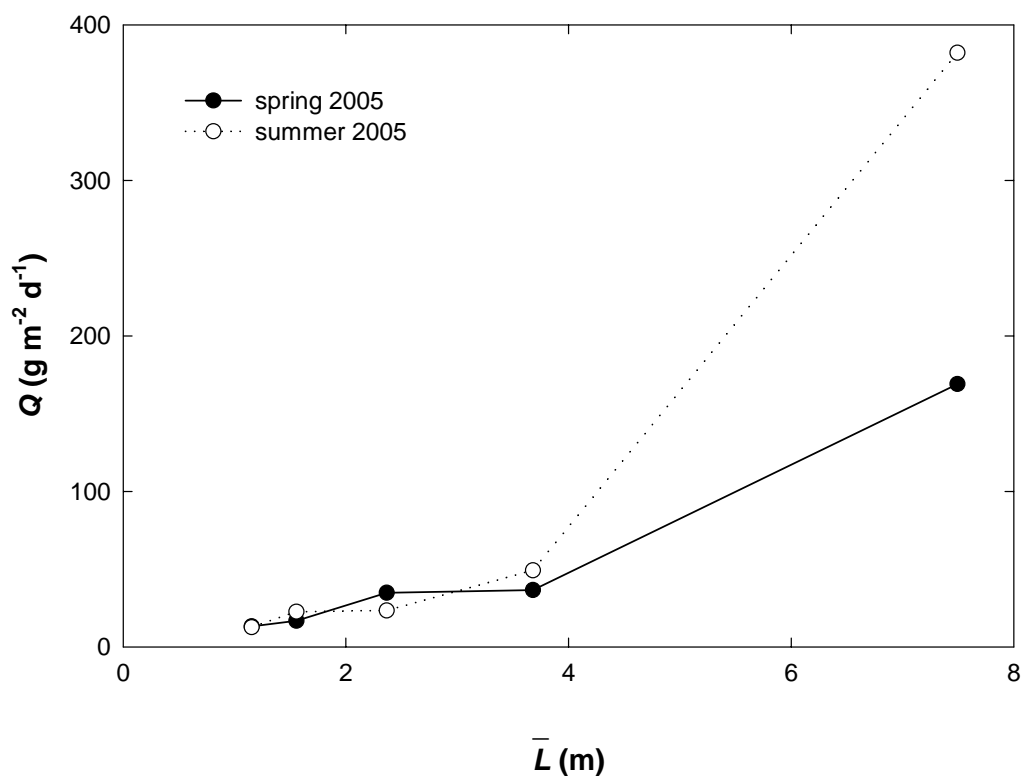
Figure 5. Dust flux versus mean gap size observed at the Jornada Experimental Range, NM during a three month period in the spring and summer of 2005.
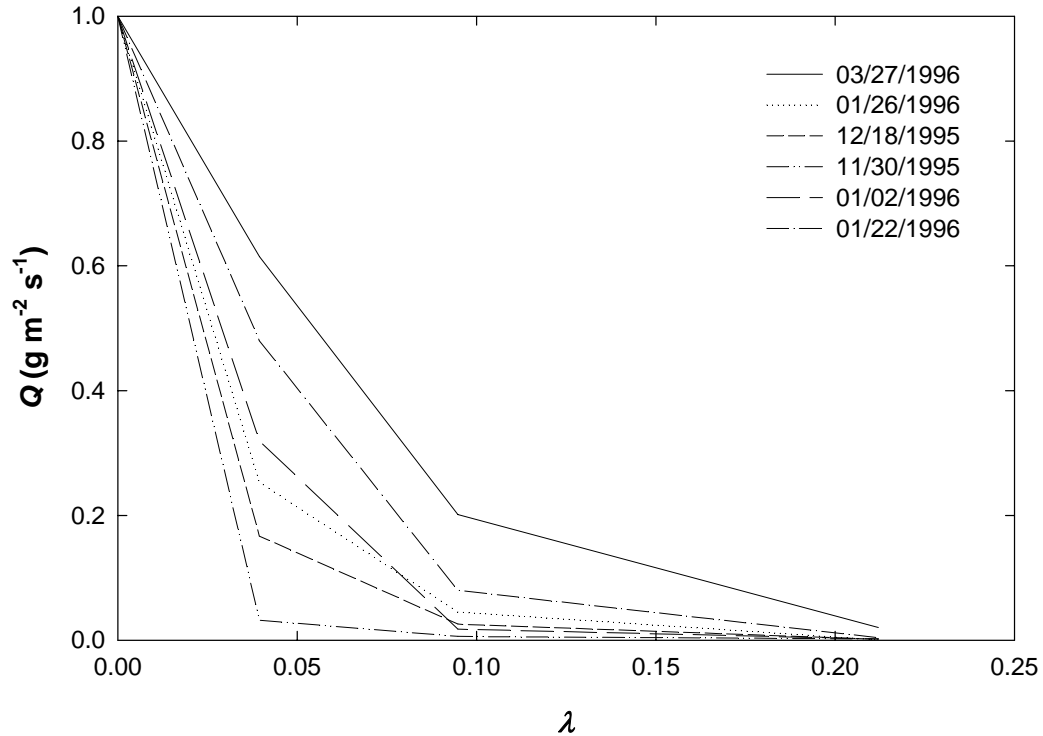
Figure 6. Flux events for lateral cover expressed in range from Owens Lake, CA (modified from Lancaster and Baas, 1998).

3. RESULTS

Estimates of Q vs. λ and Q vs. $\overline{L}$ were made with the Q=F(x) model for the

following conditions:

- Wind shear velocity: $u_* = 120$ cm s^{-1}

- Threshold shear velocity of the unvegeted soil: $u_{*ts} = 25$ cm s^{-1}

- Plant geometry: 0.5 m tall cylinders with a 1 m diameter

- Drag coefficient ratio: $\beta = 269$ calculated as C_r/C_s, C_r=0.485 (Gillies et al., 2002;
  Wyatt and Nickling, 1997), C_s=0.0018 (Marshall, 1971)

To compare results from the $Q=f(x)$ model with the existing Raupach et al. (1993) model,

we have also calculated the horizontal flux under the above conditions for constant value

of m=0.5 and m=1.0.

Three gap probability functions were used in the $Q=f(x)$ model. Presented as equations 5-7, each distribution represents different scenarios of surface vegetation (fig. 7). The majority of dust models assume homogeneous or random distributions of vegetation (Gillette and Stockton, 1989; Marticorena and Bergametti, 1995; Musick and Gillette, 1990a). In the uniform gap model, all gap sizes are assumed to have the same windward length. This scenario is unlikely due to natural variability of vegetation sizes at different times, at difference stages of growth, especially from a mosaic ecological perspective (Caylor et al., 2003), and due to inhomogeneous environmental limitations such as nutrient availability, soil moisture, and topography. However, the case of constant gap size is illustrative of how gap size influences model estimates of horizontal flux. With uniform gap spacing, flux is effectively suppressed in when the average streamwise gap width is less than 4 m or when the lateral cover exceeds 0.09.

Vegetation in natural systems is not composed of discrete sizes and constant gap distances, but of a continuous distribution of sizes and shapes. Gap size variations are represented as a normalized Poisson distribution (eq. 6). The gap distribution was normalized after eliminated distances with a probably less than 0.025. Highly variable gap sizes between plants would be expected in most natural systems due to variability in nutrient availability, soil moisture, and topography. With variable gap spacing from the Poisson distribution would be expected to demonstrate more complex behavior than the simple threshold behavior observed in the constant gap-size model. With the Poisson distribution, we observe that the decrease with lateral cover is moderated with detectible emissions at $\bar{L} > 3\,\text{m}$, and $\lambda > 0.16$. Dust emissions are expected over a wide range of average gap sizes.

A third distribution was developed from the probability of adjacent areas having the same landcover. Based on the connectivity statistic (McGlynn and Okin, 2006), a distribution similar to an exponential decay function, the gap size is calculated from the range value (eq. 7). In this approach, distances with a probability less than 0.015 were eliminated, and the distribution was normalized against the remaining lag distances. With connectivity gap spacing, dust emissions are theoretically possible at large ranges. At higher range values, the gap sizes can be as large as 30 m. Such large gaps are unlikely, due to natural constraints on vegetation. Additionally, including emissions from such high gap distances (> 20 m) is likely to overestimate dust emission in natural systems.
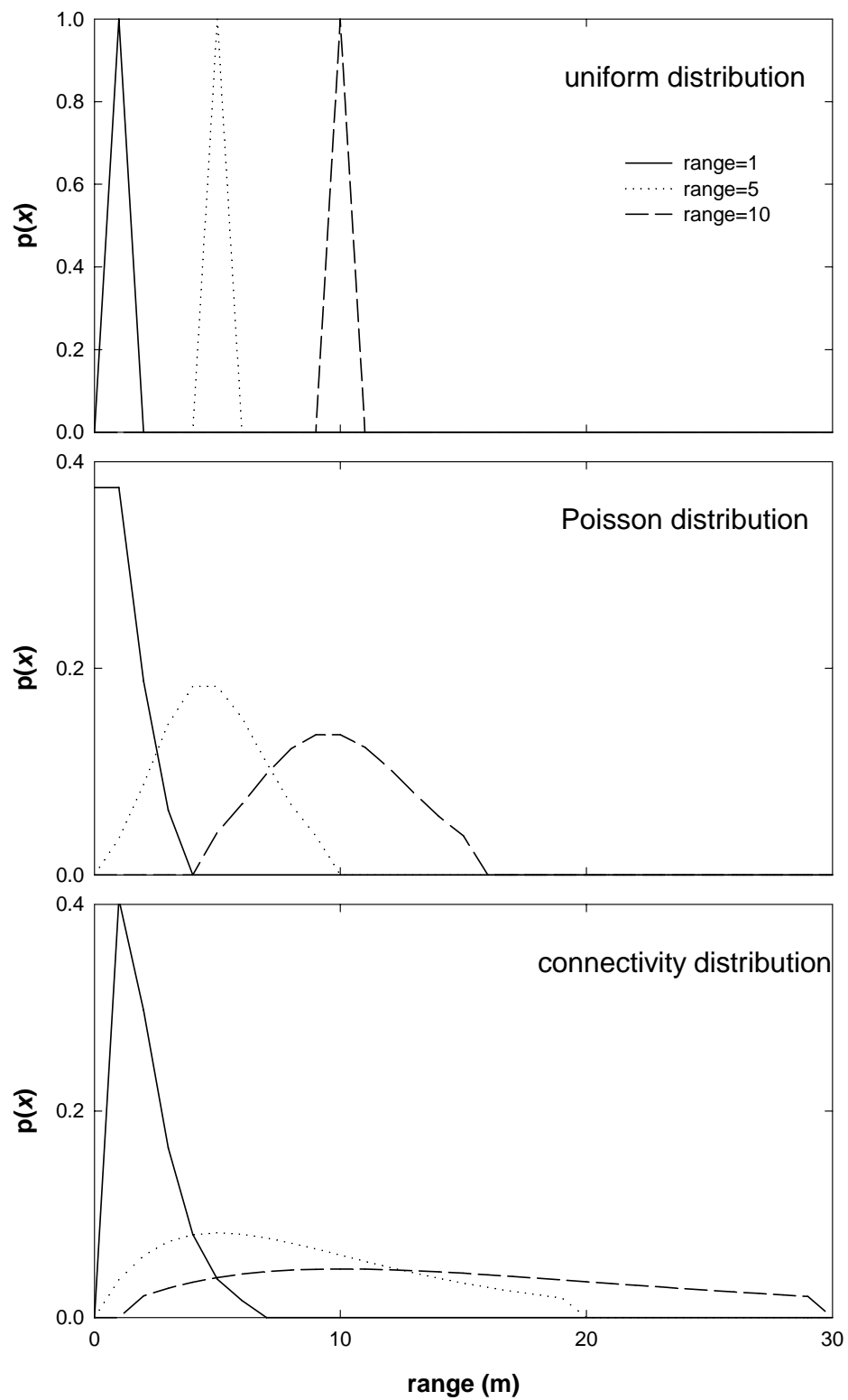
Figure 7. Gap spacing at ranges distances of 1, 7, and 10 m for uniform gap distribution, Poison gap distribution, and connectivity gap distribution.

Total flux (Q) is calculated for lateral cover based on the horizontal flux approximations (eq. 14), and the flux-probability relationship (eq. 4). In all three modeled distributions (eqs. 5-7), dust flux calculated at $u_*=150$ cm s^{-1} is highest for surfaces with minimal lateral cover (fig. 8). Flux is effectively suppressed in the uniform distribution when the average streamwise gap width is less than 4 m or when the lateral cover exceeds $\lambda = 0.09$. Dust flux is possible for almost any patch-size scale length with Poisson and connectivity distributions, and remains present beyond surfaces with high lateral cover $\lambda > 0.3$, but is greatly reduced when $\lambda \leq 0.15$.
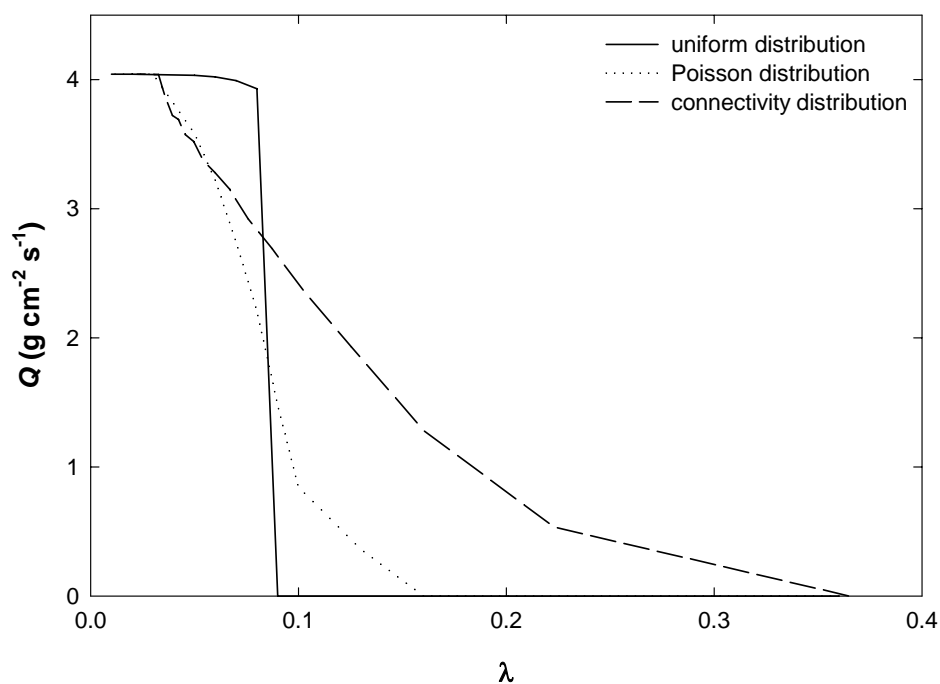
Figure 8. Probability of total dust emissions for uniform gap distribution, Poison gap distribution, and connectivity gap distribution.

Performance of the dust flux model for vegetated surfaces was evaluated against field results taken in the Jornada Experimental Range (JER), NM, and published field data from Lancaster and Baas (1998). Expressed as the ratio of dust flux relative to

maximum potential flux, high relative flux is reported from field data at $\lambda < 0.04$, with the lowest results from the mean Lancaster and Baas (1998) observations (fig. 9). Flux observations decrease sharply for JER field data with high emissions at $\lambda = 0.09$. For both sets of field data, flux emissions decrease sharply at $\lambda \approx 0.1$ as lateral cover reaches a critical density. Significant emissions are still possible at higher cover, with JER observations at $\lambda = 0.32$ and $\lambda = 0.46$. The Raupach model for a stable highly-vegetated surface ($m=1.0$) and for the recommended value from Crawley and Nickling (2003) ($m=0.55$) for low cover ($\lambda\rightarrow0$), that also approximates the Raupach value for an erodible bare surface ($m=0.5$), approximates the initial Lancaster and Baas (1998) observation at low lateral cover ($\lambda = 0.04$), but fails to account for emissions at $\lambda > 0.1$. Of the three distribution models, the uniform gap size distribution most closely matches JER field observations, but fails to predict flux probabilities at $\lambda > 0.09$. The Poisson distribution correctly matches connectivity predictions, but with higher flux estimates at high cover ($\lambda \geq 0.15$). The flux estimate for connectivity distributions accounts for emissions at high cover ($\lambda > 0.3$) but underestimates flux as $\lambda \sim 0.4$.
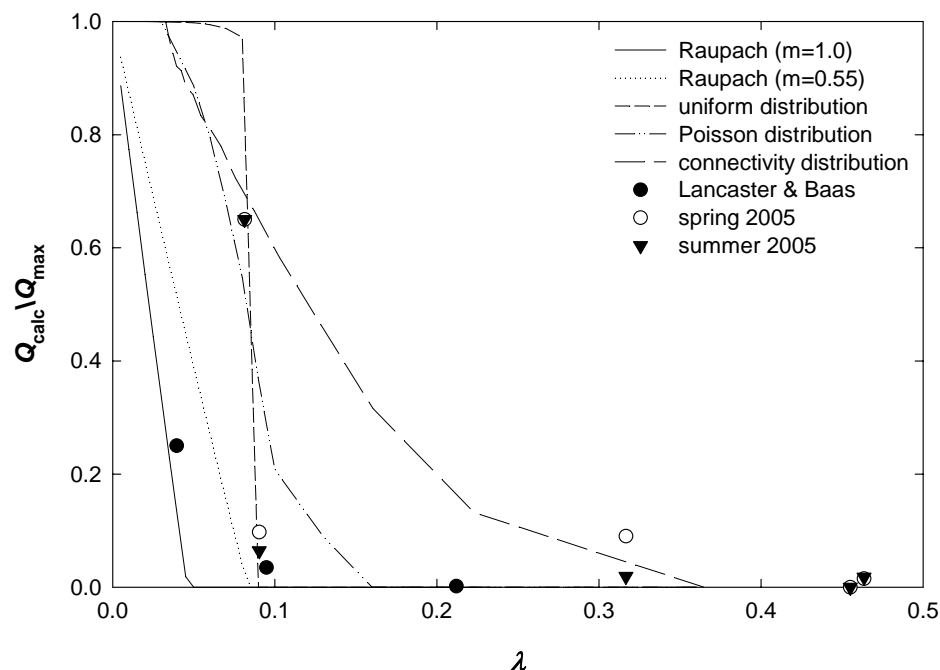
Figure 9. Dust emission models (lines) and field observations (points). Constant m models from Raupach et al. (1993) underestimate dust flux for vegetated surfaces with $\lambda > 0.2$.

When vegetation is projected as gap size, both Raupach models continuously underestimate flux probability (fig. 10). The Poisson and connectivity distributions successfully predict emissions at small gap sizes (~ 2.5 m) as observed in Lancaster and Baas (1998), and in both summer and spring 2005 JER. Only the Poison distribution accurately estimates the JER field emission with gap sizes between 3.5 and 7.5 m. In this range, the uniform distribution strongly overestimates horizontal flux, while the connectivity distribution underestimates horizontal flux.
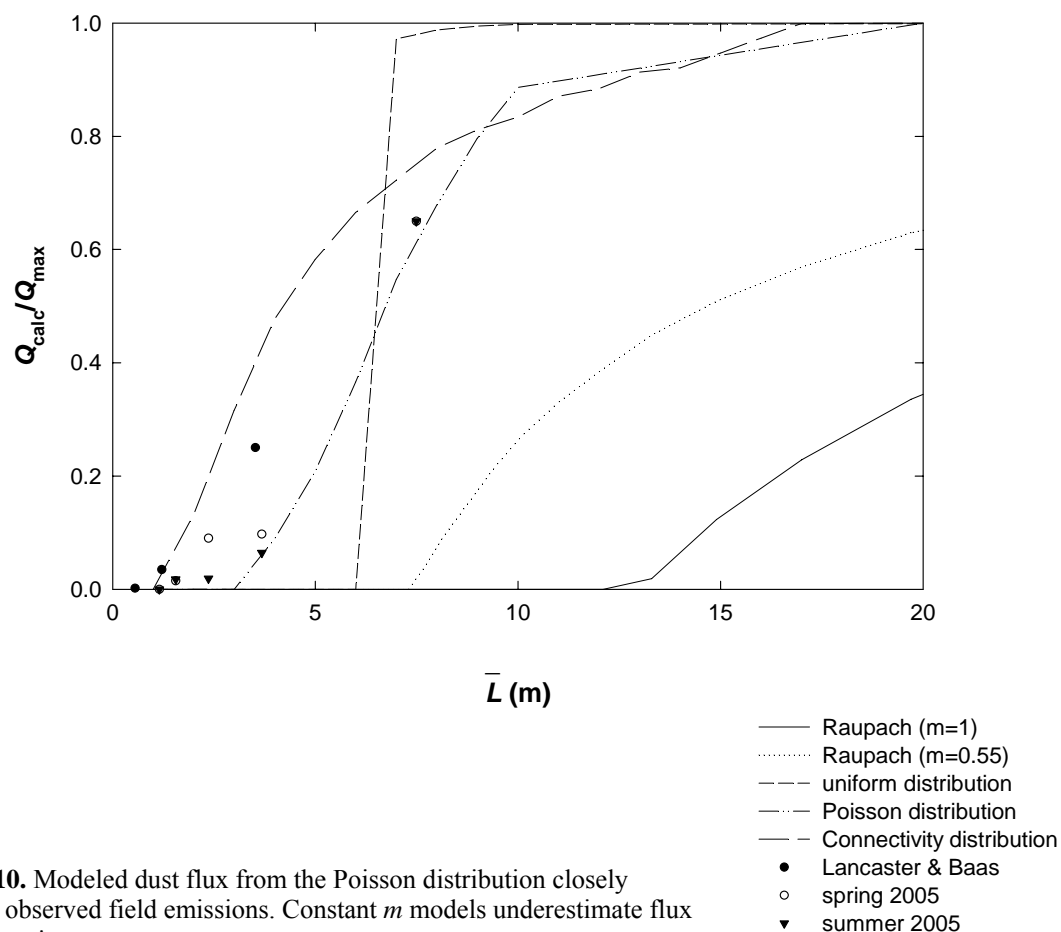
Figure 10. Modeled dust flux from the Poisson distribution closely matches observed field emissions. Constant *m* models underestimate flux for all gap sizes.

Legend:
—— Raupach (m=1)
········· Raupach (m=0.55)
– – – uniform distribution
–·–· Poisson distribution
— – Connectivity distribution
● Lancaster & Baas
○ spring 2005
▼ summer 2005

4. DISCUSSION AND CONCLUSIONS

We have presented a new model for dust flux, with shear stress inhomogeneity of vegetation for comparison with theoretical and field based experiments. The *Q=f(x)* model, based on field observations of dust flux versus mean gap size, and from published surface shear stress response to porous roughness elements, confirms surfaces stress inhomogeneity (*m*) is not constant with lateral cover and cannot be easily estimated from coarse vegetation classifications, such as bare soil, or stabilized vegetated surface. Traditional approximations of the *m* parameter are no longer valid and cannot be applied

from existing literature. Surface shear stress for vegetated surfaces was found to have a non-linear relationship with gap size suggesting possible wake interference at moderate densities of $\lambda=0.1$.

Surface roughness elements such as vegetation have long been recognized as moderators of wind erosion, affecting the erodibility of the surface and the entrainment of dust particles in arid environments. Experimental and theoretical research has demonstrated the reduction in wind erosion from vegetation by creating nonerodible surface areas, extracting wind momentum, developing downwind wakes, and capturing moving particles. A primary attribute of wind erosion reduction, is from the suppression of horizontal flux by vegetation in the form of saltation to the point where vertical dust entrainment is no longer produced.

Wind blowing over a vegetated surface is not just affected by the geometry of vegetation, but also by the spacing between plants. In surfaces with a high-density of vegetation, entrainment is greatly reduced. If the spacing between vegetation is increased, the saltation suppression of a single plant is reduced as the wind velocity and shear stress is able increase with distance, without a succeeding downwind roughness element. Field data and experimental results in figure 10 clearly demonstrate an increase in dust flux as average gap size increase on a scale from 0 to 10 m. The spacing of vegetation in most scenarios is not expected to be constant, lending more credence to the Poisson and connectivity distributions over the uniform gap size distribution, although any appropriate distribution may be applied to this model.

Incorporating vegetation gap size into the dust flux model overcomes problems associated with the use of lateral cover in the original Raupach et al. (1993) model.

Integrating the spatial distribution of vegetation with lateral cover allows a more robust representation of the surface in wind erosion that is missing from existing models.

In existing wind shear stress models (e.g., Raupach et al, 1993), the m parameter provides a proxy for inhomogenous shear stress. Nonlinear trends of m_{eff} with lateral cover imply that no single value of m can be used for a wide range of vegetation roughness densities (fig. 11).

The protective characteristics of vegetation are minimized when sparse lateral cover ($\lambda < 0.08$) and large mean gap sizes prevent overlapping shelters and wake effects from adjacent plants. In high density vegetation ($\lambda > 0.25$), a skimming flow, described in Wolfe and Nickling (1993), of continuously overlapping wake regions would also result in a relatively homogeneous surface shear stress, and even moderate distributions would have little measurable effect.

In scenarios of moderate gap sizes and lateral cover ($0.08 < \lambda < 0.25$), wake interference flow is created, producing highly inhomogeneous surface shear stress. The transitional nature of surface shear stress inhomogeneity is demonstrated as the homogeneous wind flow regime for sparse uniform vegetation becomes highly distorted with interference wakes at $\lambda = 0.8$. As λ increases to 2.5, the wakes overlap, creating large sheltered areas of homogeneous flow.
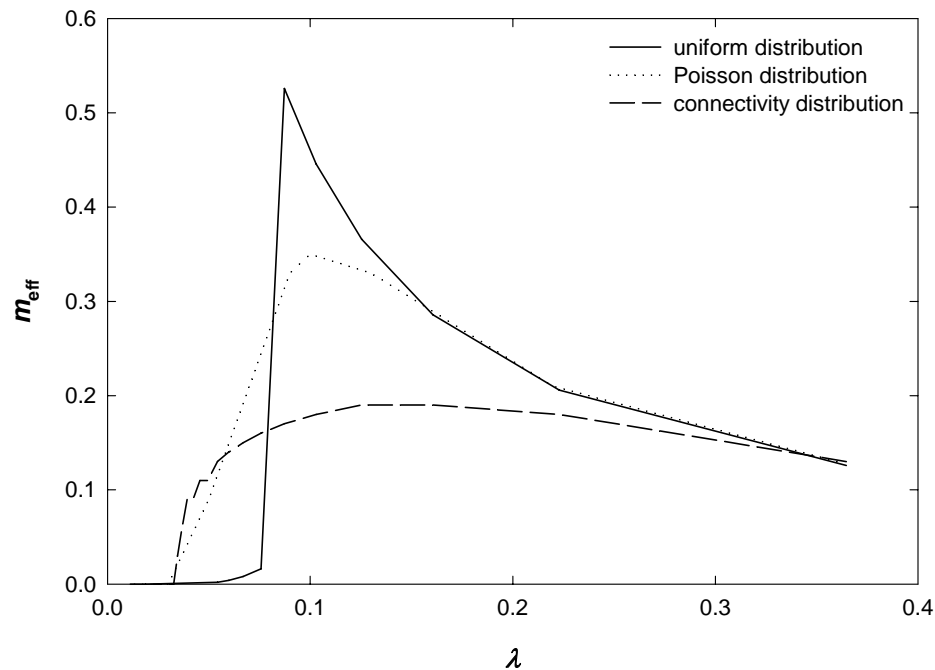
Figure 11. Natural variability in vegetation distributions in very low and high densities are minimally affect shear stress inhomogeneity while moderate densities create highly variable shear stress distributions from wake interference flow, represented with 3rd-order polynomials.

Scaling effects of inhomogeneity and vegetation distribution may account for some discrepancies between modeled dust flux and field observations. Spatially averaged calculations cannot reflect natural variation in vegetation distribution measured at a single location. Larger sample sizes may produce measured values that approximate theoretical mean spatial characteristics.

Changes in shear stress with distance and varying gap size prevent the development of a constant *m* inhomogeneity parameter. The variation in *m* parameters for seemingly similar surfaces may explain why so much research has such difficulty and inconsistency in developing practical solutions. Recent findings by King et al. (2005) suggests that shear stress partitioning overestimations require a modification of the *m* parameter from a scaling term. The semi-empirical estimation of the *m* parameter

suggested here agrees with existing field results, may represent averaged shear stress. This presents a method for consistent *m* estimations amongst literature, and could improve future dust modeling.

A larger dataset of flux emissions measured at different scales with detailed measurements of vegetation geometry and distribution is necessary to permit accurate comparison between field results and theoretical predictions. Such data may not be common, but measures of gap size from field sites, or from air and space based remote sensing imagery may enhance the predictive erodibility of vegetated surfaces.

For the present purpose, the *m* parameter is depicted as a modifier of shear stress resulting from the spatial distribution of maximum shear stress. The resulting *m* assumption, from a sigmoid fit of Bradley and Mulhearn (1983) is not based on experiments or theoretical considerations that were conducted with the intention of identifying how shear stress varies with distance from a plant. The actual shape of the $q = f(x,m)$, $m = f(x)$ function, and how it might vary with plant porosity is unknown. In addition, several assumptions for ambient conditions were used in this study as constant wind shear velocity that limit the comparison of model results with field results. Despite the general agreement from the $Q=f(x)$ model with JER field data, and with Lancaster and Baas (1998) field observations, only general predictions are possible. Detailed surface shear stress and wind records would be necessary to transition from general estimations, into accurate landscape-scale predictions and validation of this model.

CITED REFERENCES

Alfaro, S. C., and Gomes, L. (2001). Modeling mineral aerosol production by wind erosion: Emission intensities and aerosol size distributions in source areas. *Journal of Geophysical Research-Atmospheres* **106,** 18075-18084.

Ansley, R. J., Ben Wu, X., and Kramp, B. A. (2001). Observation: Long-term increases in mesquite canopy cover in a North Texas savanna. *Journal of Range Management* **54,** 171-176.

Archer, S. (1995). Tree-grass dynamics in a *prosopis-thornscrub* savanna parkland - reconstructing the past and predicting the future. *Ecoscience* **2,** 83-99.

Baatz, M., and Schäpe, A. (2000). "Multiresolution segmentation: An optimization for high quality multi-scale image segmentation." Wichmann-Verlag, Heidelberg.

Bagnold, R. A. (1941). "The physics of blown sand and desert dunes." Methuen & Co., London.

Bahre, C. J., and Shelton, M. L. (1993). Historic vegetation change, mesquite increases, and climate in Southeastern Arizona. *Journal of Biogeography* **20,** 489-504.

Baker, A. R., Jickells, T. D., Witt, M., and Linge, K. L. (2006). Trends in the solubility of iron, aluminium, manganese and phosphorus in aerosol collected over the Atlantic Ocean. *Marine Chemistry* **98,** 43-58.

Baret, F., and Guyot, G. (1991). Potentials and limits of vegetation indexes for LAI and APAR assessment. *Remote Sensing of Environment* **35,** 161-173.

Bellouin, N., Boucher, O., Haywood, J., and Reddy, M. S. (2005). Global estimate of aerosol direct radiative forcing from satellite measurements. *Nature* **438,** 1138-1141.

Bishop, J. K. B., Davis, R. E., and Sherman, J. T. (2002). Robotic observations of dust storm enhancement of carbon biomass in the North Pacific. *Science* **298,** 817-821.

Bour, O., and Davy, P. (1998). On the connectivity of three-dimensional fault networks. *Water Resources Research* **34,** 2611-2622.

Bradley, B. A., and Mustard, J. F. (2005). Identifying land cover variability distinct from land cover change: Cheatgrass in the Great Basin. *Remote Sensing of Environment* **94,** 204-213.

Bradley, E. F., and Mulhearn, P. J. (1983). Development of velocity and shear stress distributions in the wake of a porous shelter fence. *Journal of Wind Engineering and Industrial Aerodynamics* **15,** 145-156.

Buffington, L. C., and Herbel, C. H. (1965). Vegetational changes on a semidesert grassland range from 1858 to 1963. *Ecological Monographs* **35,** 139-164.

Bullard, J. E. (1997). A note on the use of the "Fryberger Method" for evaluating potential sand transport by wind. *Journal of Sedimentary Research* **67,** 499-501.

Cabral, A. C., De Miguel, J. M., Rescia, A. J., Schmitz, M. F., and Pineda, F. D. (2003). Shrub encroachment in Argentinean savannas. *Journal of Vegetation Science* **14,** 145-152.

Caylor, K. K., Dowty, P. R., Shugart, H. H., and Ringrose, S. (2004). Relationship between small-scale structural variability and simulated vegetation productivity across a regional moisture gradient in southern Africa. *Global Change Biology* **10,** 374-382.

Caylor, K. K., Shugart, H. H., Dowty, P. R., and Smith, T. M. (2003). Tree spacing along the Kalahari transect in southern Africa. *Journal of Arid Environments* **54,** 281-296.

Chadwick, O. A., Derry, L. A., Vitousek, P. M., Huebert, B. J., and Hedin, L. O. (1999). Changing sources of nutrients during four million years of ecosystem development. *Nature* **397,** 491-497.

Cleugh, H. A. (1998). Effects of windbreaks on airflow, microclimates and crop yields. *Agroforestry Systems* **41,** 55-84.

Cornelis, W. M., and Gabriels, D. (2003). The effect of surface moisture on the entrainment of dune sand by wind: an evaluation of selected models. *Sedimentology* **50,** 771-790.

Cotner, J. B., Ammerman, J. W., Peele, E. R., and Bentzen, E. (1997). Phosphorus-limited bacterioplankton growth in the Sargasso Sea. *Aquatic Microbial Ecology* **13,** 141-149.

Crawley, D. M., and Nickling, W. G. (2003). Drag partition for regularly-arrayed rough surfaces. *Boundary-Layer Meteorology* **107,** 445-468.

D'Odorico, P., Porporato, A., and Ridolfi, L. (2001). Transition between stable states in the dynamics of soil development. *Geophysical Research Letters* **28,** 595-598.

Deutsch, C. V., and Journel, A. G. (1998). "GSLIB. Geostatistical software library and users guide." Oxford University Press, New York.

Diaz, J. P., Exposito, F. J., Torres, C. J., Herrera, F., Prospero, J. M., and Romero, M. C. (2001). Radiative properties of aerosols in Saharan dust outbreaks using ground-

based and satellite data: Applications to radiative forcing. *Journal of Geophysical Research-Atmospheres* **106,** 18403-18416.

Diner, D. J., Asner, G. P., Davies, R., Knyazikhin, Y., Muller, J. P., Nolin, A. W., Pinty, B., Schaaf, C. B., and Stroeve, J. (1999). New directions in earth observing: Scientific applications of multiangle remote sensing. *Bulletin of the American Meteorological Society* **80,** 2209-2228.

Dorren, L. K. A., Maier, B., and Seijmonsbergen, A. C. (2003). Improved Landsat-based forest mapping in steep mountainous terrain using object-based classification. *Forest Ecology And Management* **183,** 31-46.

Dougill, A. J., and Thomas, A. D. (2004). Kalahari sand soils: Spatial heterogeneity, biological soil crusts and land degradation. *Land Degradation & Development* **15,** 233-242.

Dregne, H. E., and Chou, H. T. (1992). "Global desertification dimensions and costs." Texas Tech University Press, Lubbock, Texas.

Farr, T. G., and Chadwick, O. A. (1996). Geomorphic processes and remote sensing signatures of alluvial fans in the Kun Lun mountains, China. *Journal of Geophysical Research-Planets* **101,** 23091-23100.

Fensham, R. J., Fairfax, R. J., and Archer, S. R. (2005). Rainfall, land use and woody vegetation cover change in semi-arid Australian savanna. *Journal of Ecology* **93,** 596-606.

Geneletti, D., and Gorte, B. G. H. (2003). A method for object-oriented land cover classification combining Landsat TM data and aerial photographs. *International Journal of Remote Sensing* **24,** 1273-1286.

Gibbens, R. P., McNeely, R. P., Havstad, K. M., Beck, R. F., and Nolen, B. (2005). Vegetation changes in the Jornada Basin from 1858 to 1998. *Journal of Arid Environments* **61,** 651-668.

Gillette, D. (1997). Soil derived dust as a source of silica: Aerosol properties, emissions, deposition, and transport. *Journal of Exposure Analysis and Environmental Epidemiology* **7,** 303-311.

Gillette, D. A., Herbert, G., Stockton, P. H., and Owen, P. R. (1996). Causes of the fetch effect in wind erosion. *Earth Surface Processes and Landforms* **21,** 641-659.

Gillette, D. A., and Pitchford, A. M. (2004). Sand flux in the northern Chihuahuan desert, New Mexico, USA, and the influence of mesquite-dominated landscapes. *Journal of Geophysical Research-Earth Surface* **109**.

Gillette, D. A., and Stockton, P. H. (1989). The effect of nonerodible particles on wind erosion of erodible surfaces. *Journal of Geophysical Research-Atmospheres* **94,** 12885-12893.

Gillies, J. A., Nickling, W. G., and King, J. (2002). Drag coefficient and plant form response to wind speed in three plant species: Burning Bush (*Euonymus alatus*), Colorado Blue Spruce (*Picea pungens glauca.*), and Fountain Grass (*Pennisetum setaceum*). *Journal of Geophysical Research-Atmospheres* **107,** doi:10.1029/2001JD001259.

Gomes, L., Bergametti, G., Coudegaussen, G., and Rognon, P. (1990). Submicron desert dusts - a sandblasting process. *Journal of Geophysical Research-Atmospheres* **95,** 13927-13935.

Greeley, R., and Iversen., J. D. (1985). "Wind as a geological process: on Earth, Mars, Venus, and Titan." Cambridge University Press, Cambridge.

Haywood, J., and Boucher, O. (2000). Estimates of the direct and indirect radiative forcing due to tropospheric aerosols: A review. *Reviews of Geophysics* **38,** 513-543.

Houghton, J. T., Ding, Y., Griggs, D. J., Noguer, M., van der Linden, P. J., Dia, X., Maskell, K., and Johnson, C. A. (2001). "Climate change 2001: the scientific basis: contribution of Working Group I to the third assessment report of the Intergovernmental Panel on Climate." Cambridge University Press, New York.

Huete, A., Didan, K., Miura, T., Rodriguez, E. P., Gao, X., and Ferreira, L. G. (2002). Overview of the radiometric and biophysical performance of the MODIS vegetation indices. *Remote Sensing of Environment* **83,** 195-213.

Husar, R. B., Prospero, J. M., and Stowe, L. L. (1997). Characterization of tropospheric aerosols over the oceans with the NOAA advanced very high resolution radiometer optical thickness operational product. *Journal of Geophysical Research-Atmospheres* **102,** 16889-16909.

Karyampudi, V. M., Palm, S. P., Reagen, J. A., Fang, H., Grant, W. B., Hoff, R. M., Moulin, C., Pierce, H. F., Torres, O., Browell, E. V., and Melfi, S. H. (1999). Validation of the Saharan dust plume conceptual model using lidar, Meteosat, and ECMWF data. *Bulletin of the American Meteorological Society* **80,** 1045-1075.

Kaufman, Y. J., Tanre, D., and Boucher, O. (2002). A satellite view of aerosols in the climate system. *Nature* **419,** 215-223.

King, J., Nickling, W. G., and Gillies, J. A. (2005). Representation of vegetation and other nonerodible elements in aeolian shear stress partitioning models for predicting transport threshold. *Journal of Geophysical Research-Earth Surface* **110,** doi:10.1029/2004JF000281.

King, M. D., Kaufman, Y. J., Tanre, D., and Nakajima, T. (1999). Remote sensing of tropospheric aerosols from space: Past, present, and future. *Bulletin of the American Meteorological Society* **80,** 2229-2259.

Krishnan, S., and Journel, A. G. (2003). Spatial connectivity: From variograms to multiple-point measures. *Mathematical Geology* **35,** 915-925.

Laliberte, A. S., Rango, A., Havstad, K. M., Paris, J. F., Beck, R. F., McNeely, R., and Gonzalez, A. L. (2004). Object-oriented image analysis for mapping shrub encroachment from 1937 to 2003 in southern New Mexico. *Remote Sensing of Environment* **93,** 198-210.

Lancaster, N., and Baas, A. (1998). Influence of vegetation cover on sand transport by wind: Field studies at Owens Lake, California. *Earth Surface Processes and Landforms* **23,** 69-82.

Leys, J. F., and McTainsh, G. H. (1996). Sediment fluxes and particle grain-size characteristics of wind-eroded sediments in southeastern Australia. *Earth Surface Processes and Landforms* **21,** 661-671.

Li, J., Okin, G. S., Hartman, L. J., and Epstein, H. E. (submitted). Quantitative assessment of wind erosion and soil nutrient loss in desert grasslands of the southwestern United States. *Biogeochemistry*.

Li, X., Maring, H., Savoie, D., Voss, K., and Prospero, J. M. (1996). Dominance of mineral dust in aerosol light-scattering in the North Atlantic trade winds. *Nature* **380,** 416-419.

Liao, H., and Seinfeld, J. H. (1998). Effect of clouds on direct aerosol radiative forcing of climate. *Journal of Geophysical Research-Atmospheres* **103,** 3781-3788.

Liao, H., Yung, Y. L., and Seinfeld, J. H. (1999). Effects of aerosols on tropospheric photolysis rates in clear and cloudy atmospheres. *Journal of Geophysical Research-Atmospheres* **104,** 23697-23707.

Mahowald, N. M., Baker, A. R., Bergametti, G., Brooks, N., Duce, R. A., Jickells, T. D., Kubilay, N., Prospero, J. M., and Tegen, I. (2005). Atmospheric global dust cycle and iron inputs to the ocean. *Global Biogeochemical Cycles* **19,** doi:10.1029/2004GB002402.

Marshall, J. K. (1971). Drag measurements in roughness arrays of varying density and distribution. *Agricultural Meteorology* **8,** 269-292.

Marticorena, B., and Bergametti, G. (1995). Modeling the atmospheric dust cycle.1. Design of a soil-derived dust emission scheme. *Journal of Geophysical Research-Atmospheres* **100,** 16415-16430.

McGlynn, I. O., and Okin, G. S. (2006). Characterization of shrub distribution using high spatial resolution remote sensing: Ecosystem implications for a former Chihuahuan Desert grassland. *Remote Sensing of Environment* **101,** 554-566.

McNaughton, K. G. (1988). Effects of windbreaks on turbulent transport and microclimate. *Agriculture Ecosystems & Environment* **22-3,** 17-39.

Miller, R. L., Perlwitz, J., and Tegen, I. (2004). Feedback upon dust emission by dust radiative forcing through the planetary boundary layer. *Journal of Geophysical Research-Atmospheres* **109,** doi:10.1029/2003GL018279.

Musick, H., and Gillette, D. (1990a). Field evaluation of relationships between a vegetations structural parameter and sheltering against wind erosion. *Land Degredation Rehab.* **2,** 87-94.

Musick, H. B., and Gillette, D. A. (1990b). Field evaluation of relationships between a vegetation structural parameter and sheltering against wind erosion. *Land Degradation and Rehabilitation* **2,** 87-94.

Okin, G. S. (2005). Dependence of wind erosion and dust emission on surface heterogeneity: Stochastic modeling. *Journal of Geophysical Research-Atmospheres* **110,** doi:10.1029/2004JD005288.

Okin, G. S., and Gillette, D. A. (2001). Distribution of vegetation in wind-dominated landscapes: Implications for wind erosion modeling and landscape processes. *Journal of Geophysical Research-Atmospheres* **106,** 9673-9683.

Okin, G. S., Mahowald, N., Chadwick, O. A., and Artaxo, P. (2004). Impact of desert dust on the biogeochemistry of phosphorus in terrestrial ecosystems. *Global Biogeochemical Cycles* **18,** doi:10.1029/2003GB002145.

Okin, G. S., Murray, B., and Schlesinger, W. H. (2001a). Degradation of sandy arid shrubland environments: observations, process modelling, and management implications. *Journal of Arid Environments* **47,** 123-144.

Okin, G. S., and Painter, T. H. (2004). Effect of grain size on remotely sensed spectral reflectance of sandy desert surfaces. *Remote Sensing of Environment* **89,** 272-280.

Okin, G. S., Roberts, D. A., Murray, B., and Okin, W. J. (2001b). Practical limits on hyperspectral vegetation discrimination in arid and semiarid environments. *Remote Sensing of Environment* **77,** 212-225.

Phinn, S., Franklin, J., Hope, A., Stow, D., and Huenneke, L. (1996). Biomass distribution mapping using airborne digital video imagery and spatial statistics in a semi-arid environment. *Journal of Environmental Management* **47,** 139-164.

Poggi, D., Katul, G. G., and Albertson, J. D. (2004). A note on the contribution of dispersive fluxes to momentum transfer within canopies. *Boundary-Layer Meteorology* **111,** 615.

Privette, J. L., Tian, Y., Roberts, G., Scholes, R. J., Wang, Y., Caylor, K. K., Frost, P., and Mukelabai, M. (2004). Vegetation structure characteristics and relationships of Kalahari woodlands and savannas. *Global Change Biology* **10,** 281-291.

Prospero, J. M., and Lamb, P. J. (2003). African droughts and dust transport to the Caribbean: Climate change implications. *Science* **302,** 1024-1027.

Pye, K. (1987). "Aeolian Dust and Dust Deposits." Academic Press, London.

Rango, A., Chopping, M., Ritchie, J., Havstad, K., Kustas, W., and Schmugge, T. (2000). Morphological characteristics of shrub coppice dunes in desert grasslands of southern New Mexico derived from scanning LIDAR. *Remote Sensing of Environment* **74,** 26-44.

Rango, A., Goslee, S., Herrick, J., Chopping, M., Havstad, K., Huenneke, L., Gibbens, R., Beck, R., and McNeely, R. (2002). Remote sensing documentation of historic rangeland remediation treatments in southern New Mexico. *Journal of Arid Environments* **50,** 549-572.

Raupach, M. R. (1991). Vegetation-atmosphere interaction in homogeneous and heterogeneous terrain - Some implications of mixed-layer dynamics. *Vegetatio* **91,** 105-120.

Raupach, M. R. (1992). Drag and drag partition on rough surfaces. *Boundary-Layer Meteorology* **60,** 375-395.

Raupach, M. R. (1994). Simplified expressions for vegetation roughness length and zero-plane displacement as functions of canopy height and area index. *Boundary-Layer Meteorology* **71,** 211-216.

Raupach, M. R., Gillette, D. A., and Leys, J. F. (1993). The effect of roughness elements on wind erosion threshold. *Journal of Geophysical Research-Atmospheres* **98,** 3023-3029.

Raupach, M. R., and Lu, H. (2004). Representation of land-surface processes in aeolian transport models. *Environmental Modelling & Software* **19,** 93-112.

Raupach, M. R., Woods, N., Dorr, G., Leys, J. F., and Cleugh, H. A. (2001). The entrapment of particles by windbreaks. *Atmospheric Environment* **35,** 3373-3383.

Ravi, S., and D'Odorico, P. (2005). A field-scale analysis of the dependence of wind erosion threshold velocity on air humidity. *Geophysical Research Letters* **32,** doi:10.1029/2005GL023675.

Ravi, S., D'Odorico, P., Over, T. M., and Zobeck, T. M. (2004). On the effect of air humidity on soil susceptibility to wind erosion: The case of air-dry soils. *Geophysical Research Letters* **31,** doi:10.1029/2004GL019485.

Ravi, S., Zobeck, T. M., Over, T. M., Okin, G. S., and D'Odorico, P. (in press). On the effect of moisture bonding forces in air-dry soils on threshold friction velocity of wind erosion. *Sedimentology*.

Renshaw, C. E. (1999). Connectivity of joint networks with power law length distributions. *Water Resources Research* **35,** 2661-2670.

Reyes-Reyes, G., Baron-Ocampo, L., Cuali-Alvarez, I., Frias-Hernandez, J. T., Olalde-Portugal, V., Fregoso, L. V., and Dendooven, L. (2002). C and N dynamics in soil from the central higlands of Mexico as affected by mesquite (*Prosopis spp.*) and huizache (*Acacia tortuoso*): a laboratory investigation. *Applied Soil Ecology* **19,** 27-34.

Reynolds, J. F., Virginia, R. A., Kemp, P. R., de Soyza, A. G., and Tremmel, D. C. (1999). Impact of drought on desert shrubs: Effects of seasonality and degree of resource island development. *Ecological Monographs* **69,** 69-106.

Roques, K. G., O'Connor, T. G., and Watkinson, A. R. (2001). Dynamics of shrub encroachment in an African savanna: relative influences of fire, herbivory, rainfall and density dependence. *Journal of Applied Ecology* **38,** 268-280.

Rosenfeld, D., Rudich, Y., and Lahav, R. (2001). Desert dust suppressing precipitation: A possible desertification feedback loop. *PROCEEDINGS OF THE NATIONAL ACADEMY OF SCIENCES OF THE UNITED STATES OF AMERICA* **98,** 5975-5980.

Sanudo-Wilhelmy, S. A., Kustka, A. B., Gobler, C. J., Hutchins, D. A., Yang, M., Lwiza, K., Burns, J., Capone, D. G., Raven, J. A., and Carpenter, E. J. (2001).

Phosphorus limitation of nitrogen fixation by Trichodesmium in the central Atlantic Ocean. *Nature* **411,** 66-69.

Satheesh, S. K., Moorthy, K. K., Kaufman, Y. J., and Takemura, T. (2006). Aerosol optical depth, physical properties and radiative forcing over the Arabian Sea. *Meteorology and Atmospheric Physics* **91,** 45-62.

Scanlon, T. M., Caylor, K. K., Manfreda, S., Levin, S. A., and Rodriguez-Iturbe, I. (2005). Dynamic response of grass cover to rainfall variability: Implications for the function and persistence of savanna ecosystems. *Advances in Water Resources* **28,** 291-302.

Schlesinger, W. H., and Gramenopoulos, N. (1996). Archival photographs show no climate-induced changes in woody vegetation in the Sudan, 1943-1994. *Global Change Biology* **2,** 137-141.

Schlesinger, W. H., and Pilmanis, A. M. (1998). Plant-soil interactions in deserts. *Biogeochemistry* **42,** 169-187.

Schlesinger, W. H., Reynolds, J. F., Cunningham, G. L., Huenneke, L. F., Jarrell, W. M., Virginia, R. A., and Whitford, W. G. (1990). Biological feedbacks in global desertification. *Science* **247,** 1043-1048.

Scholes, R. J., Frost, P. G. H., and Tian, Y. H. (2004). Canopy structure in savannas along a moisture gradient on Kalahari sands. *Global Change Biology* **10,** 292-302.

Shao, Y., Raupach, M. R., and Findlater, P. A. (1993). Effect of saltation bombardment on the entrainment of dust by wind. *Journal of Geophysical Research-Atmospheres* **98,** 12719-12726.

Sokolik, I. N., and Toon, O. B. (1996). Direct radiative forcing by anthropogenic airborne mineral aerosols. *Nature* **381,** 681-683.

Sokolik, I. N., and Toon, O. B. (1999). Incorporation of mineralogical composition into models of the radiative properties of mineral aerosol from UV to IR wavelengths. *Journal of Geophysical Research-Atmospheres* **104,** 9423-9444.

Swap, R., Garstang, M., Greco, S., Talbot, R., and Kallberg, P. (1992). Saharan dust in the Amazon Basin. *Tellus Series B-Chemical and Physical Meteorology* **44,** 133-149.

Tanre, D., Kaufman, Y. J., Herman, M., and Mattoo, S. (1997). Remote sensing of aerosol properties over oceans using the MODIS/EOS spectral radiances. *Journal of Geophysical Research-Atmospheres* **102,** 16971-16988.

Tegen, I., Hollrig, P., Chin, M., Fung, I., Jacob, D., and Penner, J. (1997). Contribution of different aerosol species to the global aerosol extinction optical thickness: Estimates from model results. *Journal of Geophysical Research-Atmospheres* **102,** 23895-23915.

Tegen, I., Lacis, A. A., and Fung, I. (1996). The influence on climate forcing of mineral aerosols from disturbed soils. *Nature* **380,** 419-422.

Torres, O., Bhartia, P. K., Herman, J. R., Sinyuk, A., Ginoux, P., and Holben, B. (2002). A long-term record of aerosol optical depth from TOMS observations and comparison to AERONET measurements. *Journal of the Atmospheric Sciences* **59,** 398-413.

Warner, J., and Twomey, S. (1967). The production of cloud nuclei by cane fires and the effect on cloud droplet concentration. *Journal of the Atmospheric Sciences* **24,** 704-706.

Weeks, R. J., Smith, M., Pak, K., Li, W. H., Gillespie, A., and Gustafson, B. (1996). Surface roughness, radar backscatter, and visible and near-infrared reflectance in Death Valley, California. *Journal of Geophysical Research-Planets* **101,** 23077-23090.

Western, A. W., Bloschl, G., and Grayson, R. B. (1998). How well do indicator variograms capture the spatial connectivity of soil moisture? *Hydrological Processes* **12,** 1851-1868.

Whitford, W. G. (1992). Biogeochemical consequences of desertification. *ACS Symposium Series* **483,** 352-359.

Wolfe, S. A., and Nickling, W. G. (1993). The protective role of sparse vegetation In wind erosion. *Progress in Physical Geography* **17,** 50-68.

Wurzler, S., Reisin, T. G., and Levin, Z. (2000). Modification of mineral dust particles by cloud processing and subsequent effects on drop size distributions. *Journal of Geophysical Research-Atmospheres* **105,** 4501-4512.

Wyatt, V. E., and Nickling, W. G. (1997). Drag and shear stress partitioning in sparse desert creosote communities. *Canadian Journal of Earth Sciences* **34,** 1486-1498.